70-21,792

SMITH, James Alan, 1942-
A TEST OF THE $|\Delta I| = 1/2$ RULE IN LAMBDA DECAY.

The Univeristy of Michigan, Ph.D., 1970
Physics, elementary particles

University Microfilms, A XEROX Company, Ann Arbor, Michigan

THIS DISSERTATION HAS BEEN MICROFILMED EXACTLY AS RECEIVED

# A TEST OF THE $|\Delta\vec{I}| = \frac{1}{2}$ RULE IN LAMBDA DECAY

by

James Alan Smith

A dissertation submitted in partial fulfillment
of the requirements for the degree of
Doctor of Philosophy in
The University of Michigan
1970

Doctoral Committee:

Professor Oliver E. Overseth, Chairman
Professor Wilfred Kaplan
Professor Michael Longo
Associate Professor Yukio Tomozawa
Associate Professor Jens Zorn

ABSTRACT

A TEST OF THE $|\Delta\vec{I}| = \frac{1}{2}$ RULE IN LAMBDA DECAY

by

James Alan Smith

Chairman: Oliver E. Overseth

The asymmetry parameter $\alpha_o$ for $\Lambda^o \to n\pi^o$ has been measured relative to $\alpha_-$ by comparing the neutron distribution to the proton distribution from the decay $\Lambda^o \to p\pi^-$ for polarized $\Lambda^o$ hyperons. The polarized lambda particles were produced in liquid deuterium by the reaction $\pi^+ + n + (p) \to K^+ + \Lambda^o + (p)$, where (p) represents the spectator proton. A sample of 4760 neutron events and 8500 proton events gave $\alpha_o / \alpha_- = 0.977 \pm 0.071$, in good agreement with the $|\Delta\vec{I}| = \frac{1}{2}$ rule.

The spark chamber-scintillation counter experiment was performed at the Princeton-Pennsylvania Accelerator.

ACKNOWLEDGEMENTS

I would like to acknowledge the continual guidance and encouragement of my thesis advisor, Dr. Oliver Overseth, in all aspects of my work. I have found working on an experiment of this magnitude to be much like searching the seashore for shells washed up by the waves. Many times your hand will close upon something only to find it is a piece of driftwood or pebble. Dr. Overseth's experience was of inestimable value in pointing out the best coves in which to look and in helping me discriminate shells from worthless flotsam.

I have been fortunate in benefiting from the excellent instruction I received from the many teachers I have had in my long career as a student. Each in his own way contributed to my development and tried to pass on the very best he had. I am similarly grateful for many friends who shared their own insight with me over a quiet cup of coffee or a noisy work session.

I would like to thank my collaborators, Dr. Pondrom, Dr. Handler, and Dr. Limon, from the University of Wisconsin for their invaluable contribution to the planning and execution of this experiment.

I would particularly like to thank Dr. Stephen Olsen from the University of Wisconsin not only for his major contribution to the success of this experiment but for his friendship as well. We have spent many hours in discussing

and debating various aspects of this work and we have also shared many enjoyable moments.

I am grateful to Dr. Walter Wales, Mr. Jack Kellock, and the Princeton-Pennsylvania Accelerator staff for their expert skill and cooperation in performing this experiment.

Finally, I would like to dedicate this thesis to my loving wife, Sharon. She made this thesis possible not only by the things she did but by her sacrifice and understanding for the many nights I spent working on this project.

TABLE OF CONTENTS


| | | Page |
|---|---|---|
| ACKNOWLEDGEMENTS | | ii |
| LIST OF TABLES | | v |
| LIST OF FIGURES | | vi |
| I. | INTRODUCTION | 1 |
| II. | PHENOMENOLOGICAL DESCRIPTION | 4 |
| | A. THE $\lvert\Delta\vec{I}\rvert = \frac{1}{2}$ RULE TEST IN LAMBDA DECAY | 4 |
| | B. DERIVATION OF EXPRESSIONS FOR S AND P $\lvert\Delta\vec{I}\rvert = 3/2$ AMPLITUDES | 8 |
| III. | APPARATUS AND EXPERIMENTAL PROCEDURE | 14 |
| | A. INCIDENT BEAM | 14 |
| | B. SPARK CHAMBERS AND ASSOCIATED COUNTERS | 20 |
| | C. ELECTRONIC TRIGGER | 28 |
| | D. OPTICS | 33 |
| | E. CALIBRATION RUNS | 35 |
| IV. | DATA REDUCTION AND ANALYSIS | 43 |
| | A. MASS SCANNING SYSTEM | 43 |
| | B. TRACK RECONSTRUCTION PROGRAMS | 50 |
| | C. KINEMATICAL ANALYSIS | 52 |
| | D. POSSIBLE BACKGROUND CONTAMINATION | 72 |
| V. | EXPERIMENTAL RESULTS | 75 |
| VI. | CONCLUSION | 78 |
| LIST OF REFERENCES | | 82 |

LIST OF TABLES


| Table | | Page |
|---|---|---|
| I. | Pion-nucleon phase shifts for lambda decay. | 7 |
| II. | Counter and spark chamber dimensions. | 22 |
| III. | Asymmetry parameters as a function of $\|\cos \omega\|$ for neutral and charged data. | 66 |
| IV. | Asymmetry ratios for time early and time late data. | 68 |
| V. | Asymmetry parameters as a function of lambda production angle. | 76 |

LIST OF FIGURES


| Figure | | Page |
|---|---|---|
| 1. | Lambda decay distribution. | 5 |
| 2. | Beam side view orthogonal angle distribution. | 16 |
| 3. | Beam top view orthogonal angle distribution. | 17 |
| 4. | Horizontal beam intersection distribution. | 18 |
| 5. | Vertical beam intersection distribution. | 19 |
| 6. | Experimental setup. | 21 |
| 7. | Neutron detector and $K^+$ chamber. | 26 |
| 8. | Neutron energy detection efficiency. | 27 |
| 9. | Analyzing power distribution. | 29 |
| 10. | Block diagram of fast logic. | 30 |
| 11. | Optical system looking downstream. | 34 |
| 12. | $K^+$ excitation curve. | 36 |
| 13. | Proton-proton coplanarity distribution. | 39 |
| 14. | Proton-proton theta difference distribution. | 40 |
| 15. | Proton-proton vertical target intersection distribution. | 41 |
| 16. | Proton-proton horizontal target intersection distribution. | 42 |
| 17. | Neutron event. | 46 |
| 18. | Schematic of neutron event. | 47 |
| 19. | Gamma-ray conversion. | 49 |
| 20. | Reconstruction of an event. | 54 |
| 21. | Lambda center of mass production angle distributions. | 56 |
| 22. | Neutron-proton scattering angle distributions. | 57 |

LIST OF FIGURES (Concluded)


| Figure | | Page |
|---|---|---|
| 23. | Lambda-proton decay angle distribution. | 59 |
| 24. | Lambda-neutron decay angle distribution. | 60 |
| 25. | Energy distributions for positive and negative $\cos \omega$ . | 62 |
| 26. | Charged asymmetry parameter as a function of lambda production angle. | 64 |
| 27. | $\cos \omega$ curves for charged and neutral data together with Monte Carlo predictions. | 65 |
| 28. | $K^+$ lifetime distributions for charged and neutral data. | 69 |
| 29. | Asymmetry parameters as a function of spark length. | 71 |

# I. INTRODUCTION

This paper describes the results of a spark chamber-scintillation counter experiment on lambda decay done at the Princeton-Pennsylvania Accelerator during the spring of 1968. The experiment represented a collaboration between the University of Michigan and the University of Wisconsin and was designed to test the $|\Delta\vec{I}| = \frac{1}{2}$ rule in the non-leptonic decay of the lambda hyperon.

The $|\Delta\vec{I}| = \frac{1}{2}$ rule is an isospin selection rule, originally suggested by Gell-Mann and Pais[1], which allows only those decay transitions which change the total isospin of the system by $\pm \frac{1}{2}$. A weaker selection rule involving the third component of the isospin, $\Delta I_3 = \pm \frac{1}{2}$, is obeyed by all known non-leptonic decays and is a consequence of the strangeness-changing property of these decays. Gell-Mann and Pais pointed out that the stricter $|\Delta\vec{I}| = \frac{1}{2}$ rule would not only imply the weaker selection rule, but could account for the large ratio observed between the transition rates for the $2\pi$ decay modes of the $K^+$ and the $K_1^o$ particles, i.e., $K^+ \rightarrow \pi^+ + \pi^o$, and $K_1^o \rightarrow 2\pi$.

It was realized immediately that the rule was not exact since the existence of the decay, $K^+ \rightarrow \pi^+ + \pi^o$, requires $\Delta I = 3/2$ amplitudes about 5% as large as the amplitudes governing the $K_1^o \rightarrow 2\pi$ decay, but it was suggested that the rule might be exact for weak interactions in the absence of electromagnetic interactions. More recent data[2] on hyperon decays

and for the non-leptonic K-meson decays also agree with the $|\Delta\vec{I}| = \frac{1}{2}$ rule at the five to ten percent level. The test of the rule in these decays, however, is sometimes complicated by the need for phase space or electromagnetic corrections which must be applied to the data and are somewhat uncertain.

At present, there is really no theoretical framework describing the weak interaction decays which compels the $|\Delta\vec{I}| = \frac{1}{2}$ rule. It is important, therefore, to determine just how exact the rule is and to search for possible violations. The non-leptonic decay of the lambda hyperon is a particularly good decay to search for violations since the lambda particle is an isospin singlet and thus allows only $\Delta I = \frac{1}{2}$ and $\Delta I = 3/2$ transitions. This leads to rather simple relations between the amplitudes for $\Lambda^0 \rightarrow p\pi^-$ and $\Lambda^0 \rightarrow n\pi^0$ as explained in Chapter II. Furthermore, phase space and radiative corrections are small and relatively straightforward to calculate.

In lambda decay the $|\Delta\vec{I}| = \frac{1}{2}$ rule predicts that the decay neutrons and protons should have the same spatial distribution in the $\Lambda^0$ rest frame with respect to the lambda polarization direction. An experiment on lambda decay was performed once before by Cork[3] and his collaborators in 1960 to test this hypothesis. In their method they measured the asymmetries of the decay pions or, in the case of the neutral mode, the gamma-rays arising from the pi-zero mode. Their results depended heavily upon Monte Carlo corrections

and for the neutral mode they had to adjust the asymmetry by a factor of three because of these corrections. Their data together with the experimental data available before the experiment described in this paper, permits $\Delta I = 3/2$ amplitudes in lambda decay as large as 20%.

It was decided, therefore, to repeat the experiment on lambda decay with greater accuracy by directly measuring the decay asymmetries of the neutrons and protons.

## II. PHENOMENOLOGICAL DESCRIPTION

### A. THE $|\Delta\vec{I}| = \frac{1}{2}$ RULE TEST IN LAMBDA DECAY

The non-leptonic decays of the lambda particle, $\Lambda^o \to n\pi^o$, and, $\Lambda^o \to p\pi^-$, may be described by S and P wave amplitudes, where S and P represent the orbital angular momentum zero and one amplitudes respectively. The details are worked out, for example, in the text by Källen[4]. For a lambda with its spin pointing up, the amplitude for decay into the $|p\pi^-\rangle$ state is,

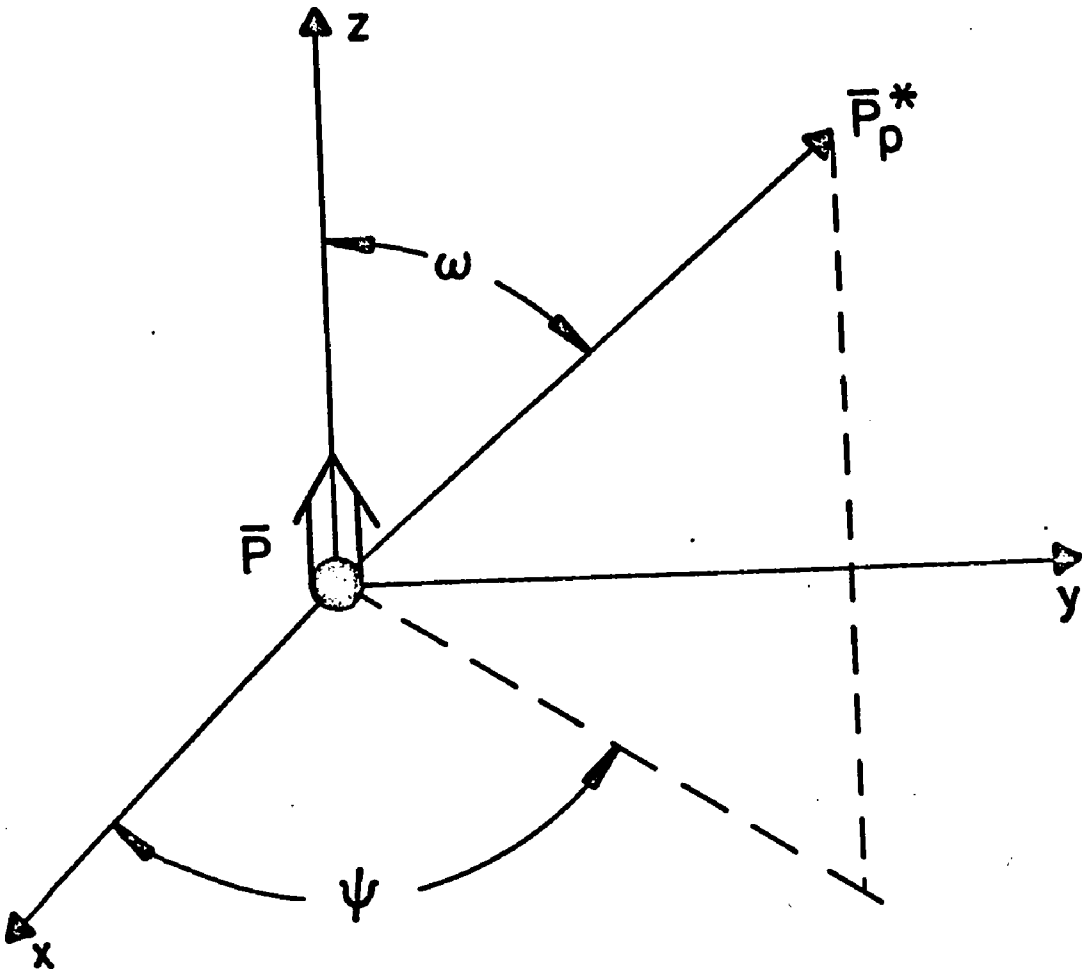
$$|\Lambda^o\uparrow\rangle = (4\pi)^{-\frac{1}{2}} \left( S^- |\uparrow\rangle + P^- (|\uparrow\rangle \cos\omega + |\downarrow\rangle \sin\omega\, e^{i\psi}) \right)$$

where, as indicated in Figure 1, $\omega$ is the angle between the lambda spin direction and the decay baryon in the rest frame of the lambda, $\psi$ is the projected azimuthal angle in the plane perpendicular to the lambda spin direction, and $|\uparrow\rangle$ and $|\downarrow\rangle$ are the spin-up and spin-down wave functions respectively. The superscript refers to the sign of the decay pion. In general, the initial state of the lambda is a statistical mixture of spin-up lambdas and spin-down lambdas and has an average polarization $\overline{P}$. The angular distribution of the decay baryon in the rest frame of the lambda is then given by,

$$N_-(\cos\omega) = 1/4\pi \left( 1 + \alpha_- \overline{P} \cos\omega \right)$$

where $\alpha_-$ is the parity-violating parameter introduced by Lee

LAMBDA REST FRAME




$$N(\cos\omega) = \frac{1}{4\pi}(1 + \alpha_- \bar{P} \cos\omega)$$

where $$\alpha_- = \frac{2\,\mathrm{Re}\,S_-^* P_-}{|S_-|^2 + |P_-|^2}$$

Fig. 1. Lambda decay distribution.

and Yang[5], i.e.,

$$\alpha_- = \frac{2\,\mathrm{Re}\,S^{-*}P^-}{|S^-|^2 + |P^-|^2} \quad .$$

The decay rate $\Gamma^-$ ( $\Lambda^o \to p\pi^-$) is given by $|S^-|^2 + |P^-|^2$. Similarly, the neutral decay may be described by $S^o$ and $P^o$ amplitudes. To investigate the predictions of the $|\Delta\vec{I}| = \frac{1}{2}$ rule, it is necessary to expand the S and P amplitudes into their $I = \frac{1}{2}$ and $I = 3/2$ components.

For $\Lambda^o \to p\pi^-$, one obtains:

$$S^- = -(2/3)^{\frac{1}{2}} S_{11} e^{i\delta 1} + (1/3)^{\frac{1}{2}} S_{33} e^{i\delta 3} \qquad (1)$$

$$P^- = -(2/3)^{\frac{1}{2}} P_{11} e^{i\delta 11} + (1/3)^{\frac{1}{2}} P_{33} e^{i\delta 31}$$

For $\Lambda^o \to n\pi^o$, one obtains:

$$S^o = (1/3)^{\frac{1}{2}} S_{11} e^{i\delta 1} + (2/3)^{\frac{1}{2}} S_{33} e^{i\delta 3} \qquad (2)$$

$$P^o = (1/3)^{\frac{1}{2}} P_{11} e^{i\delta 11} + (2/3)^{\frac{1}{2}} P_{33} e^{i\delta 31}$$

The two indices used in the subscripts refer to the quantities, $2\Delta I$ and $2I$, e.g. $S_{2\Delta I, 2I}$.

The pion-nucleon S-wave scattering phase shifts are given by $\delta_{1}$ and $\delta_{3}$; the P-wave phase shifts for $I = \frac{1}{2}$ and $I = 3/2$ at 44 MeV incident pion kinetic energy are given by $\delta_{11}$ and $\delta_{31}$ respectively. The phase shifts give the effect of the final-state strong interaction between the baryon and the outgoing pion. Roper, et. al.[6] have recently compiled all data to give these phase shifts with uncertainties

on the order of a half of a degree. The results are shown in Table I.

TABLE I

PION-NUCLEON PHASE SHIFTS FOR $\Lambda^{o}$ DECAY

| S-Wave | | P-Wave | |
|---|---|---|---|
| $\delta_1$ | $6.0^{o}$ | $\delta_{11}$ | $-1.1^{o}$ |
| $\delta_3$ | $-3.8^{o}$ | $\delta_{31}$ | $-0.7^{o}$ |

If time reversal is valid in lambda decay, $S_{11}$, $S_{33}$, $P_{11}$, $P_{33}$, and the phase shifts are real. In that case, the effect of the phase shifts would be quite small since they would then enter only as arguments of the cosine function. In later analysis, time reversal invariance will be assumed, but the effect of final state interactions will be included. It should also be pointed out that Pondrom[7] has shown that time reversal violations could allow for larger $\Delta I = 3/2$ amplitudes than would otherwise be permitted by the experimental data.

The pure $|\Delta \vec{I}| = \frac{1}{2}$ rule implies that $S_{33} = P_{33} = 0$, and thus from equations (1) and (2) that:

$$\frac{S^{o}}{S^{-}} = \frac{P^{o}}{P^{-}} = -1/\sqrt{2}$$

In the absence of radiative corrections[8], therefore, the $|\Delta\vec{I}| = \frac{1}{2}$ rule has the following predictions:

$$N_-(\cos\omega) = N_o(\cos\omega) = \frac{1}{4\pi}(1 + \alpha\overline{P}\cos\omega)$$

$$\frac{\alpha_o}{\alpha_-} = 1.0$$

$$\frac{\Gamma^o}{\Gamma^-} = 0.5$$

In the experiment described by this paper, polarized lambda particles were generated by the reaction, $\pi^+ + n \rightarrow K^+ + \Lambda^o$, and the ratio $\alpha_o / \alpha_-$ was measured directly by comparing the spatial distributions N (cos $\omega$) for the neutrons and protons from the decaying lambda hyperons.

## B. DERIVATION OF EXPRESSIONS FOR S AND P $|\Delta\vec{I}| = 3/2$ AMPLITUDES

With the S and P amplitudes given by equations (1) and (2) it is possible to derive equations for the four experimentally accessible parameters: $\alpha_-$, the charged decay asymmetry parameter, $\alpha_o/\alpha_-$, the ratio of the asymmetry parameters, $\Gamma^o/\Gamma^-$, the ratio of the decay rates, and $\Gamma^o + \Gamma^-$, the total decay rate. These four equations can then be solved for the four unknowns, $S_{11}$, $P_{11}$, $S_{33}$, and $P_{33}$. The details of this derivation will be given in this

section, and two linear equations for the ratio of the S and P $|\Delta\vec{I}| = 3/2$ amplitudes to the $|\Delta\vec{I}| = \frac{1}{2}$ amplitudes will be determined. Since no time reversal violations have been observed in lambda decay[9], time reversal invariance will be assumed. In addition, terms of second order in the $|\Delta\vec{I}| = 3/2$ amplitudes will be ignored.

The total decay rate, $\Gamma^o + \Gamma^-$, is given by:

$$\Gamma^o + \Gamma^- = |S^o|^2 + |P^o|^2 + |S^-|^2 + |P^-|^2$$

$$= S_{11}^2 + P_{11}^2 - \frac{2}{3}\sqrt{2}\, S_{11}S_{33}\cos(\delta_1 - \delta_3)$$

$$+ \frac{2}{3}\sqrt{2}\, S_{11}S_{33}\cos(\delta_1 - \delta_3)$$

$$-\frac{2}{3}\sqrt{2}\, P_{11}P_{33}\cos(\delta_{11} - \delta_{31})$$

$$+\frac{2}{3}\sqrt{2}\, P_{11}P_{33}\cos(\delta_{11} - \delta_{31}) + O^2(\Delta I = 3/2)\ ,$$

$$\Gamma^o + \Gamma^- = S_{11}^2 + P_{11}^2\ .$$

Experimentally, the rate has been measured[10] as $0.397 \pm .005 \times 10^{10}$ $\text{sec}^{-1}$. A simplification in the manipulation of the amplitudes results if the amplitudes are measured in units of $(\Gamma^o + \Gamma^-)^{\frac{1}{2}} = 0.63 \times 10^5\ \text{sec}^{-\frac{1}{2}}$. In these units,

$$S_{11}^2 + P_{11}^2 = 1\ . \qquad \text{(I)}$$

In finding the ratios of the amplitudes this common multiplicative factor will cancel.

The branching ratio into the charged and neutral modes is given by,

$$\frac{\Gamma^o}{\Gamma^-} = \frac{|S^o|^2 + |P^o|^2}{|S^-|^2 + |P^-|^2}$$

$$= \frac{S_{11}^2+P_{11}^2+2\sqrt{2}\,[S_{11}S_{33}\cos(\delta_1-\delta_3)+P_{11}P_{33}\cos(\delta_{11}-\delta_{31})]}{2(S_{11}^2+P_{11}^2)-2\sqrt{2}[S_{11}S_{33}\cos(\delta_1-\delta_3)+P_{11}P_{33}\cos(\delta_{11}-\delta_{31})]} .$$

After some rearranging, this becomes,

$$\frac{\Gamma^o}{\Gamma^-} = \tfrac{1}{2}\,[1+3\sqrt{2}\,(S_{11}S_{33}\cos(\delta_1-\delta_3)+P_{11}P_{33}\cos(\delta_{11}-\delta_{31})] \quad . \qquad \text{(II)}$$

Similarly, the asymmetry parameter for the charged decay mode,

$$\alpha_- = \frac{2\ \mathrm{Re}\ S^{-*}P^-}{|S^-|^2 + |P^-|^2}$$

becomes,

$$\alpha_- = 2S_{11}P_{11}\cos(\delta_{11}-\delta_1) \times (1+\sqrt{2}\,[S_{11}S_{33}\cos(\delta_1-\delta_3) + P_{11}P_{33}\cos(\delta_{11}-\delta_{31})] - \frac{\sqrt{2}}{2}\,[\,\frac{S_{33}\cos(\delta_{11}-\delta_3)}{S_{11}\cos(\delta_{11}-\delta_1)} + \frac{P_{33}\cos(\delta_{31}-\delta_1)}{P_{11}\cos(\delta_{11}-\delta_1)}\,]\,) \quad . \qquad \text{(III)}$$

The ratio of the asymmetry parameters becomes,

$$\frac{\alpha_o}{\alpha_-} = 1 - 3\sqrt{2}\,[S_{11}S_{33}\cos(\delta_1-\delta_3) + P_{11}P_{33}\cos(\delta_{11}-\delta_{31})] + \frac{3\sqrt{2}}{2}\left[\frac{S_{33}\cos(\delta_{11}-\delta_3)}{S_{11}\cos(\delta_{11}-\delta_1)} + \frac{P_{33}\cos(\delta_{11}-\delta_3)}{P_{11}\cos(\delta_{11}-\delta_1)}\right] \qquad \text{(IV)}$$

These four equations, I, II, III, IV, may now be solved for the four unknowns $S_{11}$, $S_{33}$, $P_{11}$, and $P_{33}$. There is also the additional information that $S_{11} > P_{11}$, since the $\gamma$ parameter[5],

$$\gamma = \frac{|S|^2 - |P|^2}{|S|^2 + |P|^2}$$

has been determined to be greater than zero[11].

Multiplying equation (III) by 3 and adding the result to equation (IV) yields,

$$\frac{3\alpha_-}{2S_{11}P_{11}\cos(\delta_{11}-\delta_1)} + \frac{\alpha_o}{\alpha_-} = 4,$$

or

$$S_{11}P_{11} = \frac{3\alpha_-}{2(4-\alpha_o/\alpha_-)\cos(\delta_{11}-\delta_1)}.$$

Solving this equation simultaneously with equation (I)

and requiring $S_{11} > P_{11}$ yields,

$$S_{11} = \left[ 1 + \left[1 - \left(\frac{3\alpha_-}{(4-\alpha_o/\alpha_-)\cos(\delta_{11}-\delta_1)}\right)^2\right]^{\frac{1}{2}}\right]^{\frac{1}{2}} \quad (3)$$

and

$$P_{11} = (1 - S_{11}^2)^{\frac{1}{2}} \quad (4)$$

Equations (I) and (II) may now be combined after some rearranging as,

$$\Delta\Gamma = \frac{3\sqrt{2}\cos(\delta_1-\delta_3)}{2[1+(P_{11}/S_{11})^2]} \frac{S_{33}}{S_{11}} + \frac{3\sqrt{2}\cos(\delta_{11}-\delta_{31})}{2[1+(S_{11}/P_{11})^2]} \frac{P_{33}}{P_{11}} \quad . \quad (5)$$

Here $\Delta\Gamma$ is the measured value of $\Gamma^o/\Gamma^-$ minus the predicted value. For a pure $|\Delta\vec{I}| = \frac{1}{2}$ rule with no corrections, the predicted value is $\frac{1}{2}$. Other predicted values will be considered in Chapter VI.

Similarly, equations (I) and (IV) may be combined to yield,

$$\Delta\alpha = 3\sqrt{2}\left[\frac{\cos(\delta_{11}-\delta_3)}{2\cos(\delta_{11}-\delta_1)} - \frac{\cos(\delta_1-\delta_3)}{1+(P_{11}/S_{11})^2}\right]\frac{S_{33}}{S_{11}} +$$

$$3\sqrt{2}\left[\frac{\cos(\delta_{31}-\delta_1)}{2\cos(\delta_{11}-\delta_1)} - \frac{\cos(\delta_{11}-\delta_{31})}{1+(S_{11}/P_{11})^2}\right]\frac{P_{33}}{P_{11}} \quad , \quad (6)$$

where $\Delta\alpha$ represents the measured value of $\alpha_o/\alpha_-$ minus the predicted value.

Thus, $\alpha_-$ and $\alpha_o/\alpha_-$ will be used to determine $S_{11}/P_{11}$ from equations (3) and (4). This ratio will then be substituted into equations (5) and (6) to yield the S and P $|\Delta\vec{I}| = 3/2$ amplitudes consistent with the experimental data.

## III. APPARATUS AND EXPERIMENTAL PROCEDURE

The lambda hyperons studied in this experiment were generated by focusing a beam of 1.0 GeV/c positive pi-mesons onto a liquid deuterium target and triggering the apparatus on the reaction, $\pi^+ + n + (p) \rightarrow \Lambda^o + K^+ + (p)$, where (p) is the spectator proton. The occurrence of this event was determined by detecting the $K^+$ mesons by means of an array of scintillation and Cherenkov counters placed to the left of the beam line looking downstream. If a charged particle were also detected to the right of the beam line, a set of spark chambers was pulsed to determine the trajectories of the particles. The spark chambers were then photographed and the photographed particle tracks were subsequently measured on the Michigan Automatic Scanning System.

### A. INCIDENT BEAM

The circulating 3.0 GeV/c internal proton beam of the Princeton-Pennsylvania Accelerator struck a platinum target and the resulting positive particles thus produced were passed through a beam transport system consisting of two 32 inch Mark I quadrupole doublets, two 16 inch Mark II quadrupoles, and two 36 inch bending magnets. The total flight path was 862.25 inches. The $\pi^+$ intensity of the beam was approximately $10^5$ pions per second; its momentum was

1.0 GeV/c $\pm$ 1.5%.

The shape of the beam was determined by recording the beam intensity using a small counter which could be moved in horizontal and vertical directions. An exposure of the beam was also periodically taken by placing a piece of unexposed polaroid film at the upstream end of the target. In addition, at the beginning of the experiment a small spark chamber was placed just behind the downstream end of the empty target and several thousand beam tracks recorded.

The beam spot at the upstream end of the target was an ellipse measuring two inches in the vertical direction and one and one-half inches in the horizontal direction. Figures 2 and 3 show the distributions of the top and side view orthogonal angles of the beam tracks as recorded in the spark chamber. These distributions indicate that the angular divergence of the beam from the nominal beam line at the target was $\pm$ 15 mr. The intersections of the beam tracks with a plane placed perpendicular to the beam direction are shown in Figures 4 and 5. These distributions indicate that the beam was centered in the horizontal direction but was actually 0.3 inches above the surveyed beam line in the vertical direction. This deduction is also indicated in the results of the proton-proton elastic scattering run discussed in Section E.

Two beam defining scintillation counters, $B_1$ and $\overline{B}_2$, were placed just upstream from a 15 inches long liquid

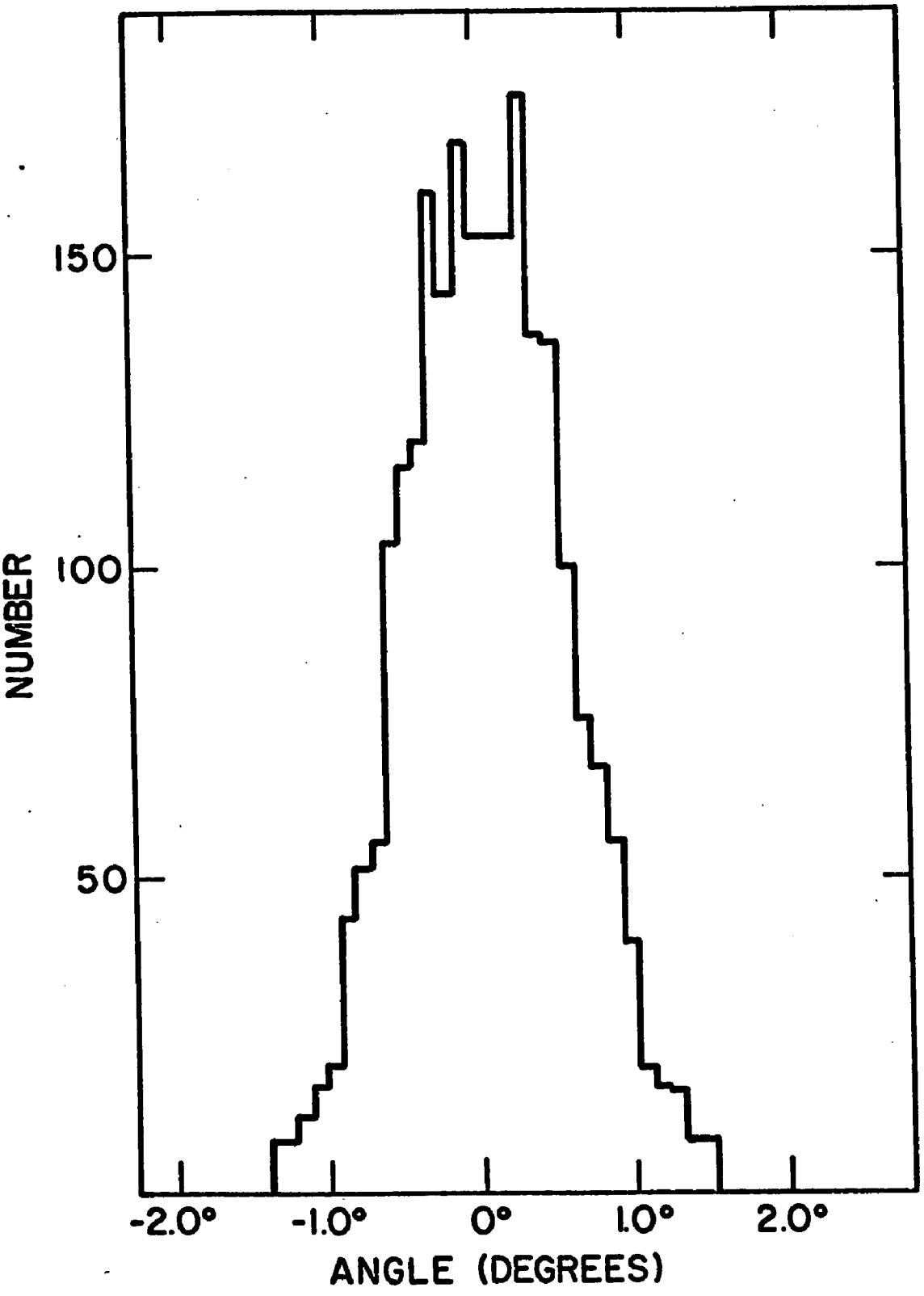



Fig. 2. Beam side view orthogonal angle distribution.

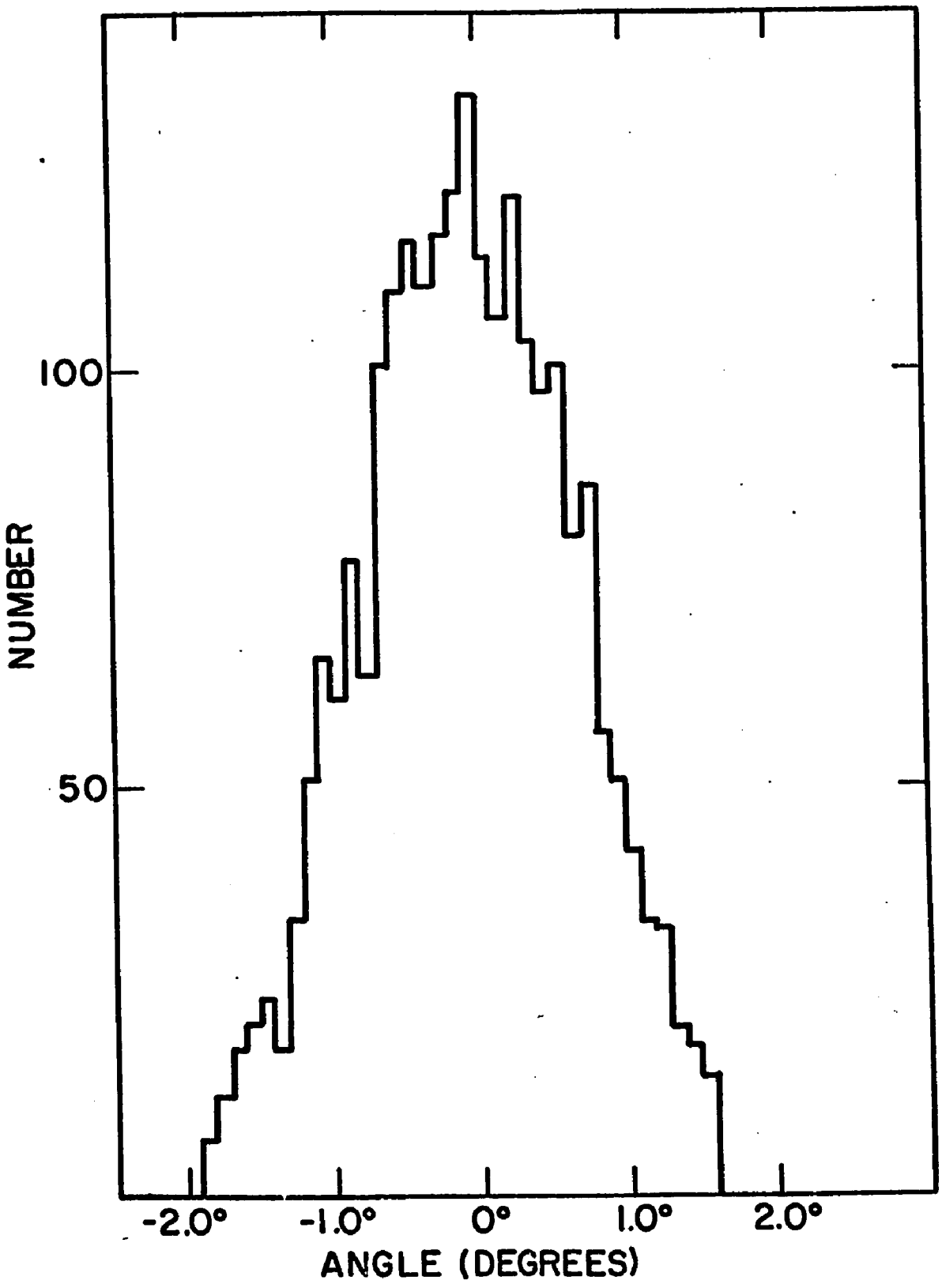



Fig. 3. Beam top view orthogonal angle distribution.

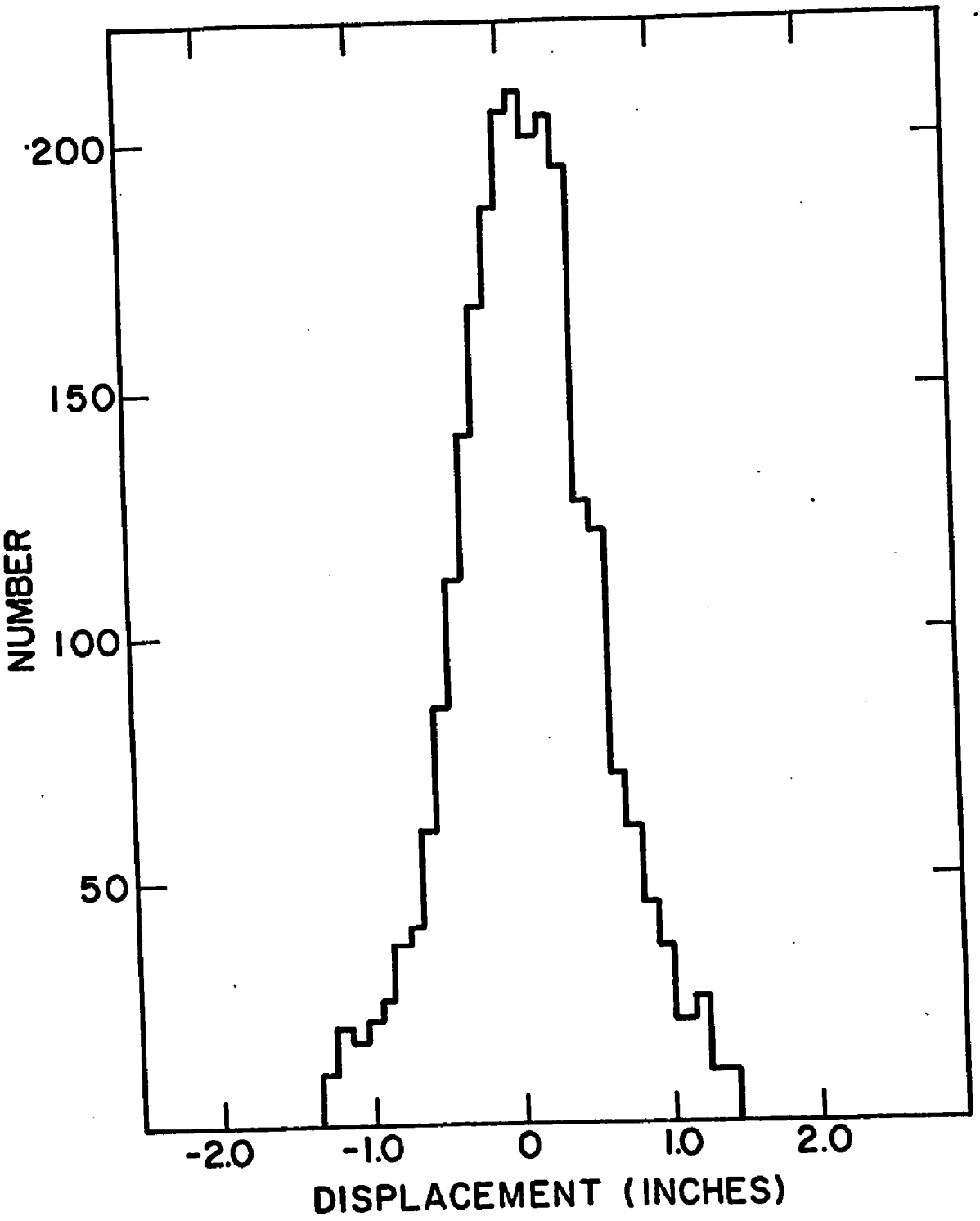



Fig. 4. Horizontal beam intersection distribution.

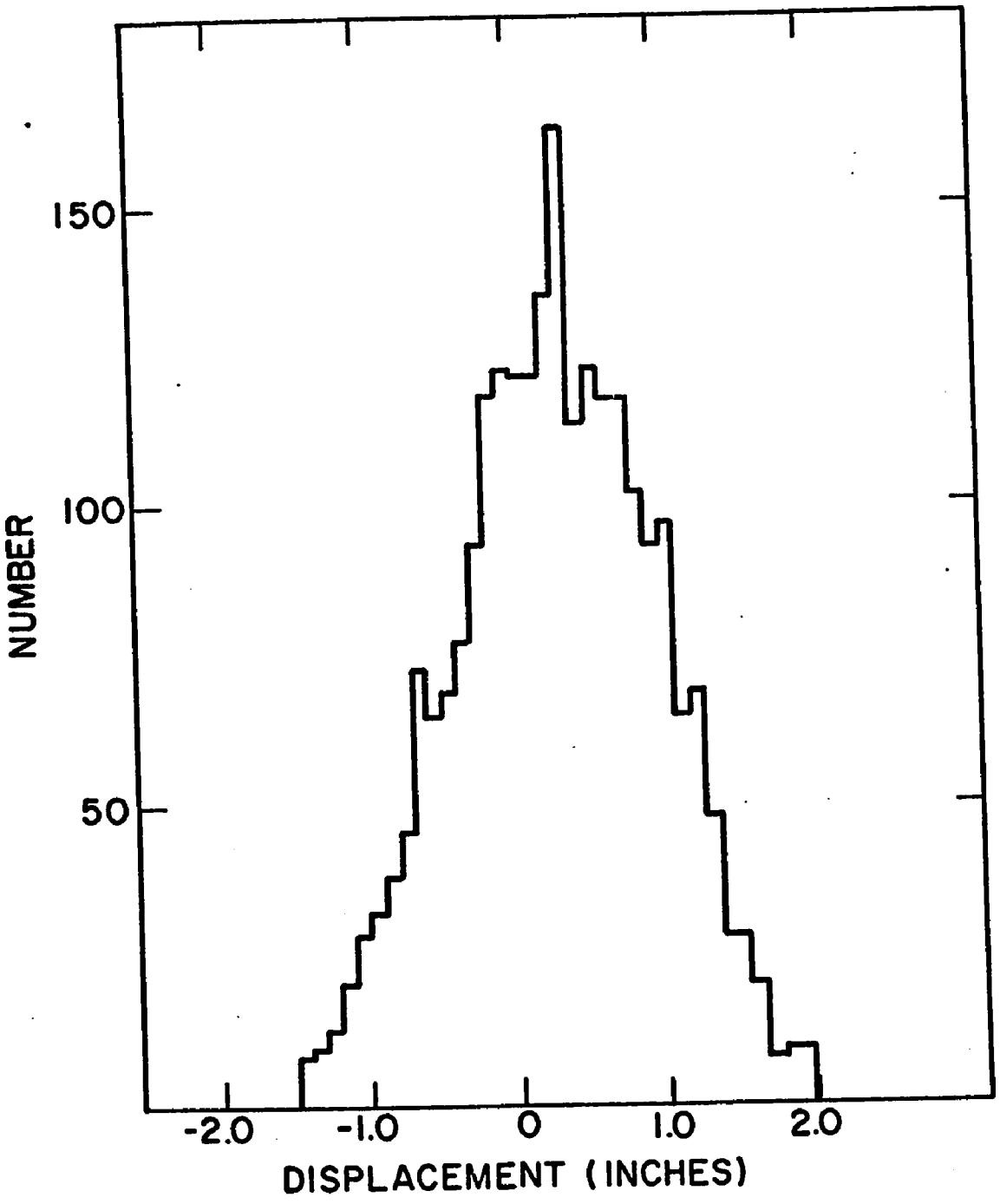



Fig. 5. Vertical beam intersection distribution.

deuterium filled target. The diameter of the target was four inches. The dimensions of $B_1$ were two inches by two inches. $\bar{B}_2$ was an anti-counter containing a hole two and one-half inches in diameter. Thus, any particle not traversing the hole generated a pulse and the event was vetoed.

The RF acceleration of the protons in the internal circulating beam of the PPA was such that they were grouped in very tight bunches 1.5 nanosecond wide and separated by 67 nanoseconds. When the internal beam was incident upon the platinum target, therefore, the resulting secondary particles were produced at known and precise intervals. This timing structure allowed us to identify the positive pi-mesons from other positive particles in the beam by measuring their time-of-flight relative to their production at the internal target. The pi-mesons came 75 nanoseconds after their production inside the machine and by triggering only on incident particles arriving in the appropriate time slot, a clean pion trigger was obtained.

## B. SPARK CHAMBERS AND ASSOCIATED COUNTERS

A schematic diagram of the experimental arrangement is shown in Figure 6 and a summary of the dimensions of the spark chambers and counters is given in Table II.

The $K^+$ telescope consisted of a two-module thin plate spark chamber, two scintillation counters, $K_1$ and $K_2$, on either side of an anticoincidence water Cherenkov

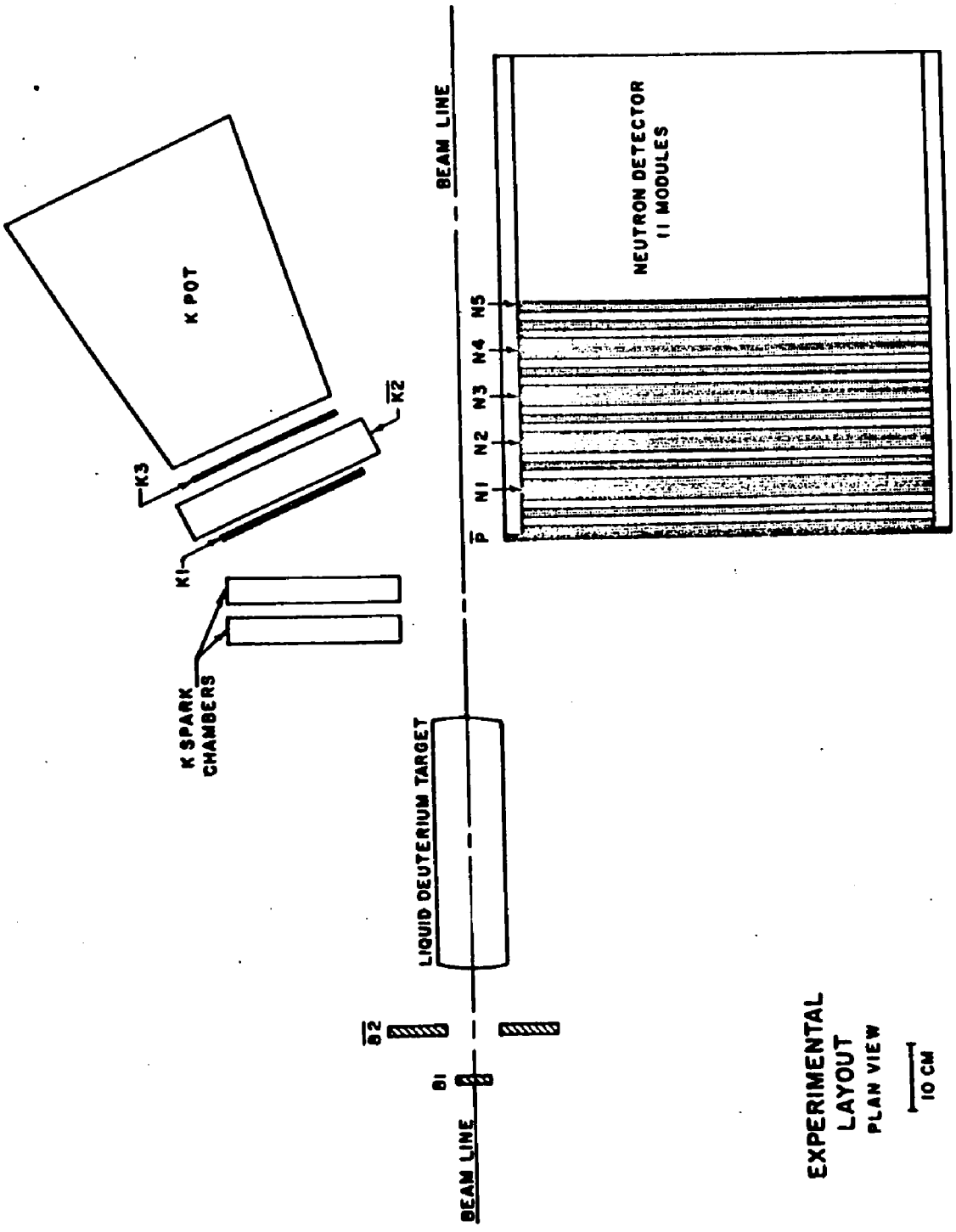



Fig. 6. Experimental setup.

TABLE II

COUNTER AND SPARK CHAMBER DIMENSIONS

| | |
|---|---|
| $K^+$ Spark Chamber | Two modules. Each containing four 3/8 inch gaps separated by thin foil Al. The active area of each module was 20 inches high x 10 inches wide x $1\frac{1}{2}$ inches thick. Modules separated by 1 5/16 inches. Positioned 33 inches from beam line and 12.7 inches from target center. |
| Neutron Spark Chamber | Eleven modules, each followed by a scintillation counter. Each module contained two 3/8 inches gaps separated by three plates of $\frac{1}{2}$ inch thick polyethylene ($CH_2$) of density 0.9 gm/cm$^3$. $CH_2$ plates were covered with 25 micron thick Al foil separated by a distance of 0.15 cm from the plates. Active area of each module was 24 inches x 24 inches. Positioned 3.9 inches from beam line and 18.5 inches from target center. |
| $K_1$, $K_2$ | $9\frac{1}{4}$ inches wide x 18 inches high x $\frac{1}{2}$ inch thick. Each viewed by a 56 AVP photomultiplier tube. |
| $\overline{K}_2$ | 20 inches high x $12\frac{1}{4}$ inches wide x $2\frac{1}{4}$ inches thick and was viewed by seven RCA 6810a photomultiplier tubes. |
| K-pot | 31 inches high at upstream end and $18\frac{1}{4}$ inches high at downstream end. $17\frac{1}{2}$ inches thick. Viewed by eleven 58 AVP photomultiplier tubes. Positioned 27.5 inches from target center. |
| $\mu$-wrap | 10 scintillation counters of assorted sizes surrounding the K-pot. Each counter was viewed by a 56 AVP tube. |
| $N_1 \cdots N_{11}$ P | Active area was 24 inches x 24 inches. Each viewed by 56 AVP tube, except P, which was viewed by two such photomultiplier tubes. |

counter, $\bar{K}_2$, a second water Cherenkov counter, called the K-pot, and ten scintillation counters, called the mu-wrap, surrounding the K-pot. The apparatus was centered in the vertical direction about a plane of symmetry bisecting the deuterium target. The $K^+$ spark chambers were placed perpendicular to the beam direction. The remaining apparatus used in the K-telescope was placed symmetrically along an axis making an angle of 25 degrees with the beam line.

The positions and orientation of the K-telescope were selected so that positive kaons with opening angles with respect to the beam of between 10 and 40 degrees would be intercepted. These kaons had energies between 80 and 220 MeV and thus moved with velocities less than 0.75 times the speed of light in vacuum and would not count in the water Cherenkov counters directly. Furthermore, approximately three fourths of the $K^+$ particles generated in the production reaction at these angles had just enough energy to pass through the $K^+$-spark chamber, the two scintillation counters, $K_1$ and $K_2$, the anti-water Cherenkov counter, $\bar{K}_2$, and then come to rest in the large K-pot. After a time delay, the $K^+$ would then decay into fast decay products, typically a positive mu-meson and a neutrino, which would emit light in the K-pot and also pass through a counter in the mu-wrap.

Thus a legitimate K particle would give a signal in $K_1$ and $K_2$ but no signal in the anti-counter, $\bar{K}_2$. After a time delay a coincidence between the K-pot and a counter in the mu-wrap would be observed. The $K^+$-spark chambers

were then pulsed to give the direction of the kaon. The distribution of the time delays between a pulse from $K_2$ and a pulse from the mu-wrap gave a measure of the $K^+$ lifetime. The use of the mu-wrap counters surrounding the K-pot was necessary to increase the time resolution of the system. The response of the K-pot alone was not sufficient to yield a sample of kaons free from background.

Elastically scattered pi-mesons produced in the reaction, $\pi^+ + n \rightarrow \pi^+ + n$, came off with velocities of the order of $\beta \approx 0.9$ and would cause a pulse in the anti-counter, $\overline{K}_2$. The pions would also pass through $K_1$ and $K_2$, the second water counter, and directly into the mu-wrap and thus appear as a prompt decay. Inefficiencies in the anti-counter, $\overline{K}_2$, would, therefore, contribute to a "prompt" peak in the life-time curve of the $K^+$ trigger. The timing distributions were also examined in the analysis of the data and served as a check on the background contamination in the data sample.

The neutron detector consisted of eleven spark chamber modules each followed by a scintillation counter. An anti-coincidence counter was positioned in front of the assembly and acted as a veto-counter when it was desired to trigger the apparatus on a neutral decay of the lambda. In addition, when triggering on neutral decays, a $\frac{1}{4}$ inch (1.3 radiation lengths) lead sheet was placed in front of the assembly to suppress gamma-rays arising from the decaying pi-zero meson. The neutron detector contained 30 gm/cm$^2$ of $CH_2$ and 3.5 gm/cm$^2$

of polystyrene or, equivalently, presented 29 gm/cm$^2$ of C and 4.5 gm/cm$^2$ of H to incident particles. A photograph of the side view of the apparatus showing both the neutron and the $K^+$ spark chambers is given in Figure 7.

Protons from the $\Lambda^o \rightarrow p + \pi^-$ decay mode were observed directly in the chamber and the range of the proton in the polyethylene material gave a measure of the proton energy. Neutrons from the $\Lambda^o \rightarrow n + \pi^o$ decay mode were detected by observing the proton recoils off the hydrogen or carbon atoms in the plates. The neutron detector was sensitive to neutrons or protons in the range of 50 to 250 MeV. Because the relevant n-p and n-C cross-sections are known in this energy range[12,13], the detection efficiency of the neutron detector could be calculated using Monte Carlo techniques. Figure 8 shows the neutron detection efficiency inferred as a function of neutron energy as calculated by my collaborators at the University of Wisconsin[14]. There is a sharp cutoff at low energies because a proton-recoil had to contain at least three sparks to be considered. The rather rapid cutoff at high energies is due to the finite chamber size and range requirement. The average detection efficiency was 12%.

Sixty percent of the proton recoils were found to be the result of a free n-p elastic scatter, while forty percent were the result of a quasi-elastic scattering off the C atoms. The recoil protons were detected with equal efficiency from both sources.

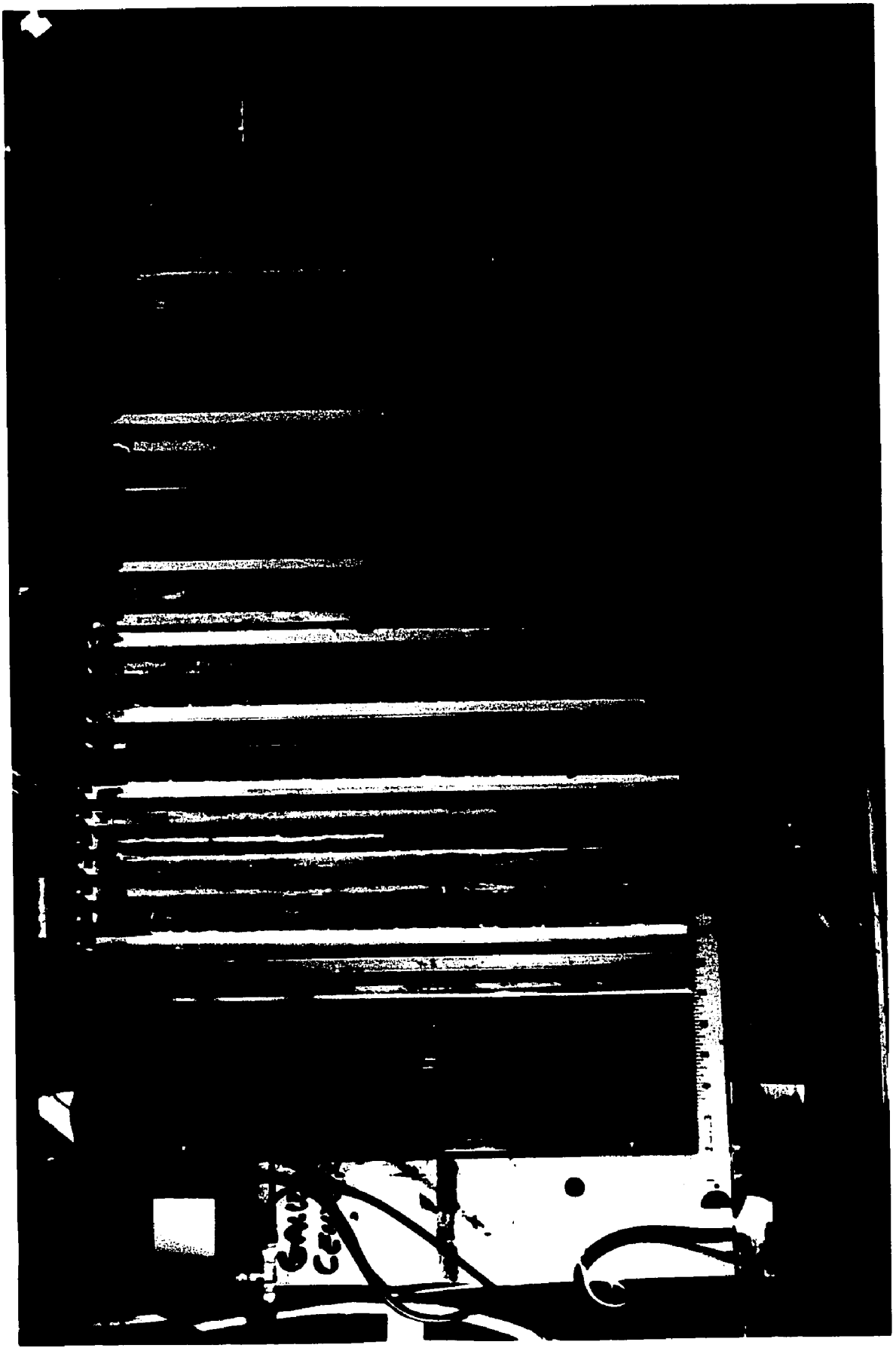


Fig. 7. Neutron detector and K° Chamber.

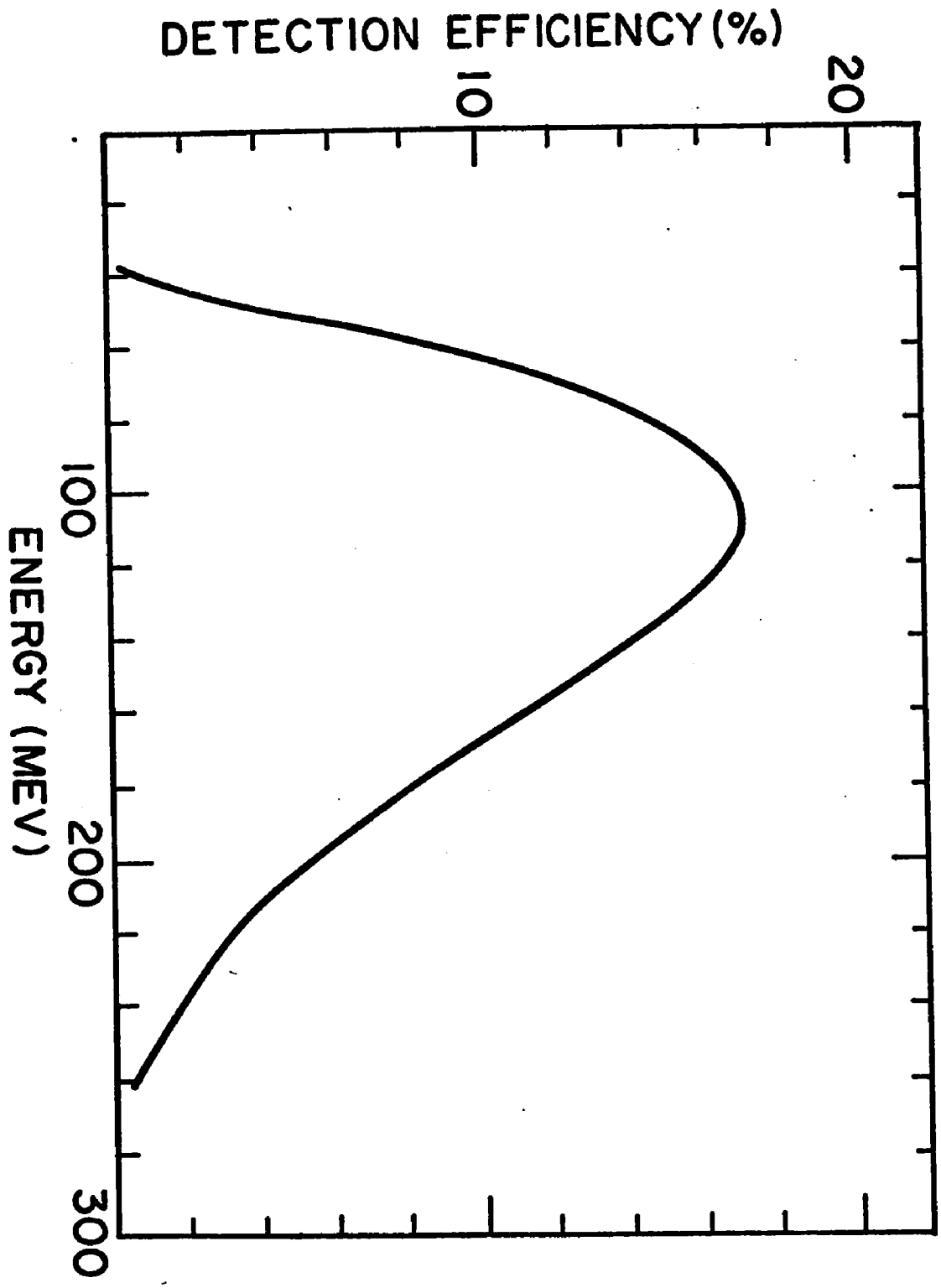



Fig. 8. Neutron energy detection efficiency.

An analyzing power curve for proton recoils detected in the chamber was also calculated assuming all the recoils came from free n-p scattering. For this analysis the Yale phase shift tables, YLAM3[15], were used. The curve is shown in Figure 9. The average analyzing power was found to be only 3.0%. The low analyzing powers correspond to n-p scatters with a large momentum transfer and these were the events detected most easily.

A more detailed description of the neutron detector construction and the Monte-Carlo simulation are given in the article by Pondrom, Olsen, and Barney[14] appearing in Nuclear Instruments and Methods.

## C. ELECTRONIC TRIGGER

A schematic diagram of the electronic triggering scheme is shown in Figure 10. A coincidence circuit is indicated by a semi-circle symbol and a discriminator, fan-in combination by a rectangle. The two beam defining counters were used in coincidence with a time delay corresponding to the time-of-flight of the pi-mesons traversing the beam line. The pulses were first fed into discriminators before entering the coincidence circuit. The resulting coincidence is labelled ($B_1\overline{B}_2RF$). The outputs of the seven photomultiplier tubes viewing the anti-coincidence counter, $\overline{K}_2$, were mixed in a fan in, fed into a linear amplifier, and then into a

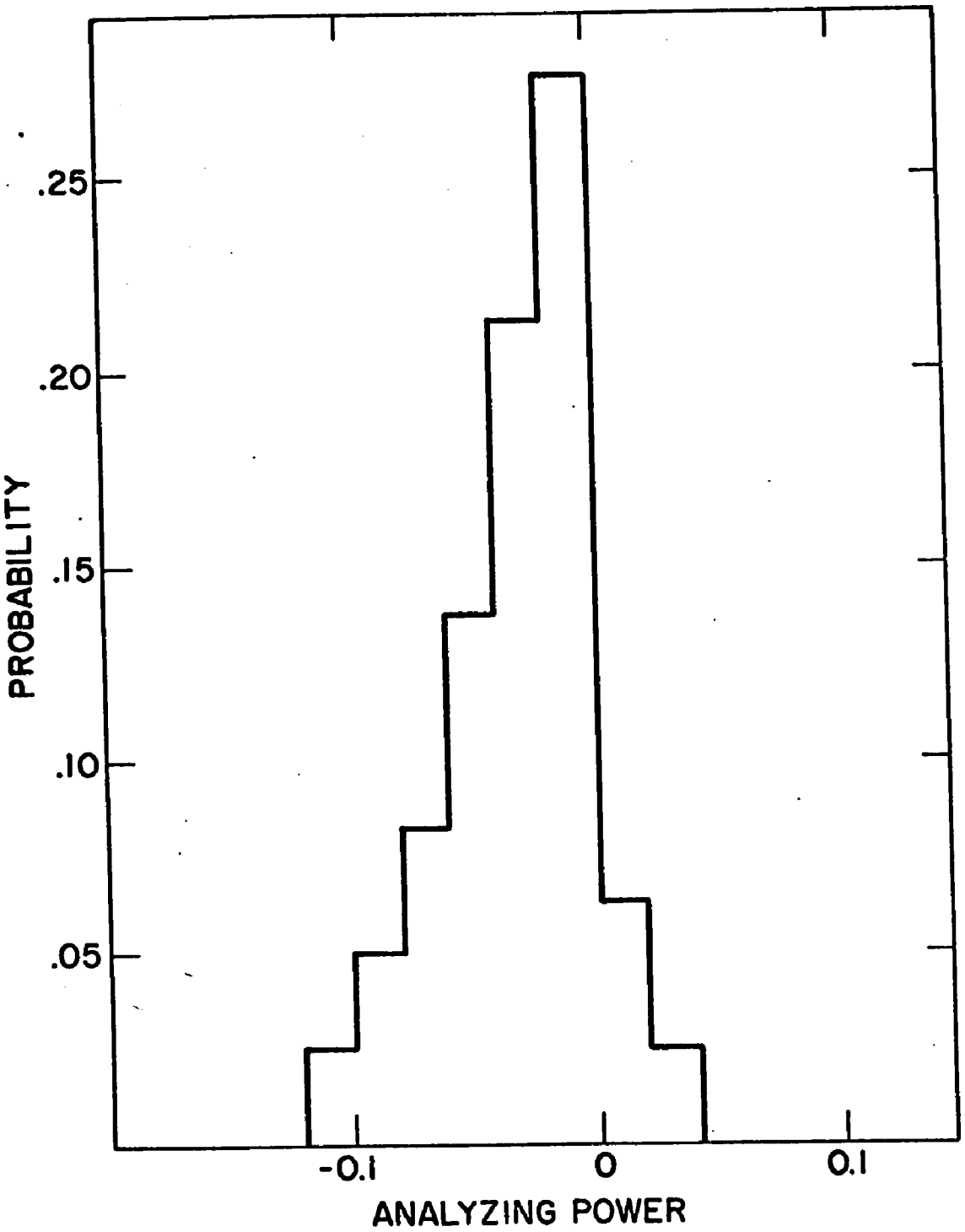



Fig. 9. Analyzing power distribution.

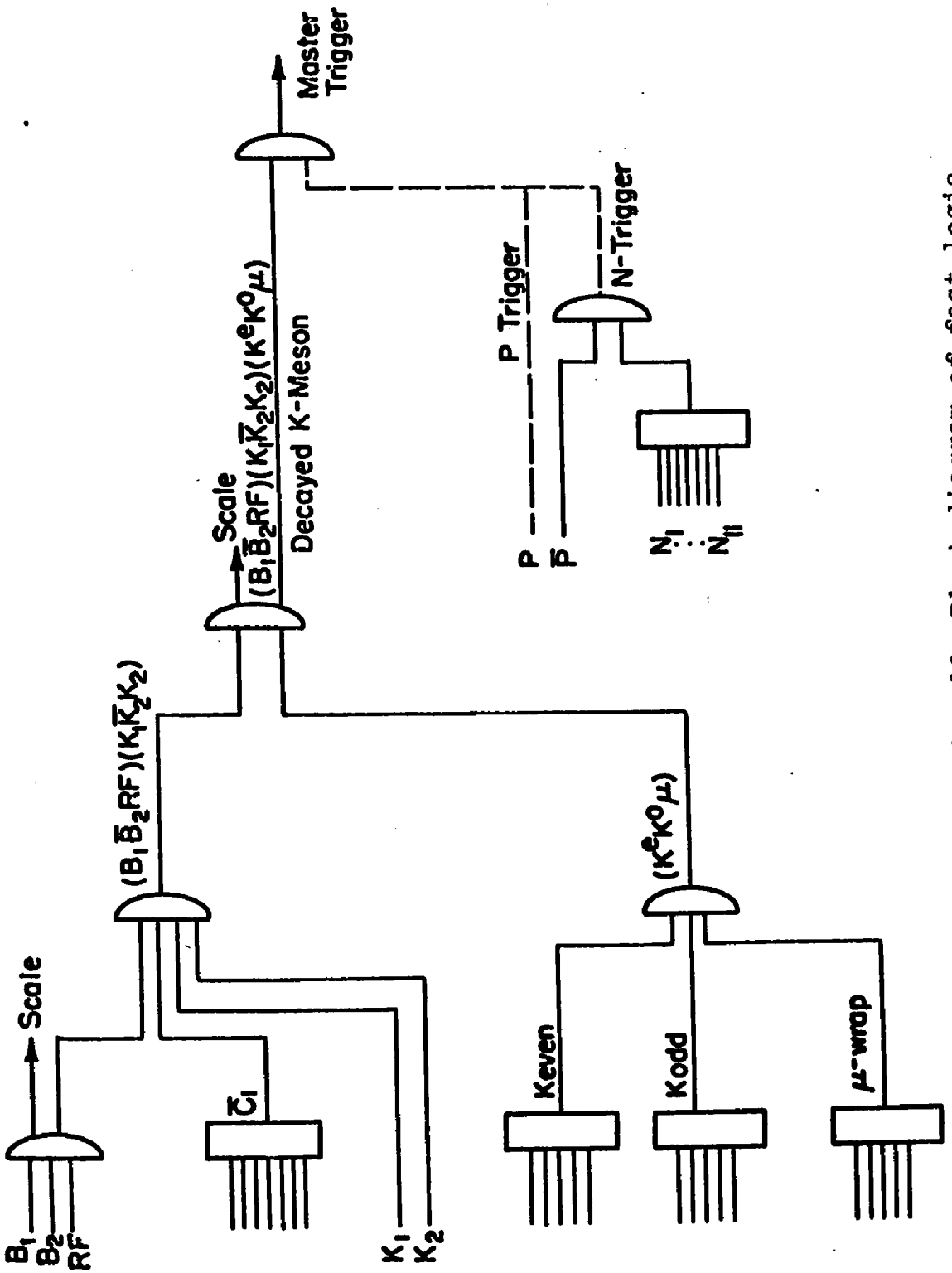



Fig. 10. Block diagram of fast logic.

discriminator. This pulse was then used in coincidence with the pulses from $K_1$, and $K_2$, and the coincidence pulse $(B_1\bar{B}_2RF)$ for a four-fold coincidence, $(B_1\bar{B}_2RF)(K_1\bar{K}_2K_2)$.

The eleven photomultiplier tubes viewing the large K-pot were mixed in two batches. Six of the tubes were mixed in one fan-in and five in a second fan-in. The output pulses of the two fan-ins are labelled K-Even, $(K^e)$, and K-Odd, $(K^o)$, in the diagram. The outputs of the mu-wraps were also fed into a fan-in and a three-fold coincidence was formed between $K^e$, $K^o$, and the mu-wrap, $(K^eK^o\mu)$. The decayed $K^+$ mesons were identified by forming a coincidence between $(B_1\bar{B}_2RF)(K_1\bar{K}_2K_2)$ and $(K^eK^o\mu)$. This coincidence was required to occur within a 60 nanosecond gate generated by the $K_1\bar{K}_2K_2$ circuit.

For the charged decay mode, the master trigger consisted of the $K^+$-telescope pulse in coincidence with the proton counter, P. For the neutral decay mode, the neutron counters, $N_1, \ldots, N_{11}$, were fed into a fan-in and the $K^+$-telescope pulse was used in coincidence with any neutron counter and in anti-coincidence with the proton anti-counter.

The time delay between $K_2$ and the mu-wrap coincidence was measured on a time-to-height converter, fed into an analog to digital converter, and stored in the core of a pulse height analyzer. The timing numbers were also displayed on the film. In addition, whenever the spark chambers were triggered, a flash lamp was pulsed for each of the

neutron scintillation counters that registered a pulse. This information was used by the scanners to aid in choosing a correct track from among possible multiple tracks which were not in coincidence with the master trigger.

The voltages of all of the scintillation counters in the experiment were adjusted so that the counters operated with an efficiency of at least 99% at various positions on the counters. The voltages were set high enough so that the efficiencies of the counters were not sensitive to voltage drifts.

The efficiency of the anti-coincidence water Cherenkov counter, $\overline{K}_2$, was checked by placing it in the beam line and triggering on either pi-mesons or protons in the beam by choosing an appropriate time delay. The counter was 99.2% efficient for detecting fast particles, i.e. pi-mesons, and counted less than 10% of the slow particles in the beam. Similarly, the efficiency of the second water-Cherenkov counter was checked by triggering on elastically-scattered pi-mesons.

The efficiencies of all the counters were checked periodically during the course of the experiment and no significant deviations were encountered.

The charged data were taken at a rate of 1 trigger per second. The neutral rate was $\frac{1}{4}$ per second.

## D. OPTICS

A schematic diagram of the optical arrangement used to view the spark chambers is shown in Figure 11. Two large field lenses, $L_1$ and $L_2$, each measuring 48 inches in diameter and having a focal length of 25 feet were placed in a top and side position as shown. The lenses insured that the camera looked directly into the chambers and eliminated any corrections for parallax. The top and side view optical paths were then folded by a symmetrical mirror arrangement. $M_1$ and $M_3$ were each placed 90 inches from the field lenses. These mirrors measured 36 inches x 40 inches. $M_2$ and $M_4$ were placed 76 inches from $M_1$ and $M_3$ and 112 inches from the camera. $M_2$ and $M_4$ were 30 inches by 20 inches.

The camera was a Flight Research Camera, Model 207-35 mm with a 120 mm focal length lens. The overall demagnification on the film was 60.

The mirrors were constructed as a honeycomb matrix; each mirror unit consisted of the 3/8 inch thick mirror glued to a slab of aluminum hexcel material which was then glued to a matching piece of plate glass. The hexcel material was three inches thick for $M_1$ and $M_3$ and one inch thick for $M_2$ and $M_4$. The mirror units were mounted in place by gripping onto the matching plate glass only. Thus, no direct pressure was ever applied to the mirror itself.

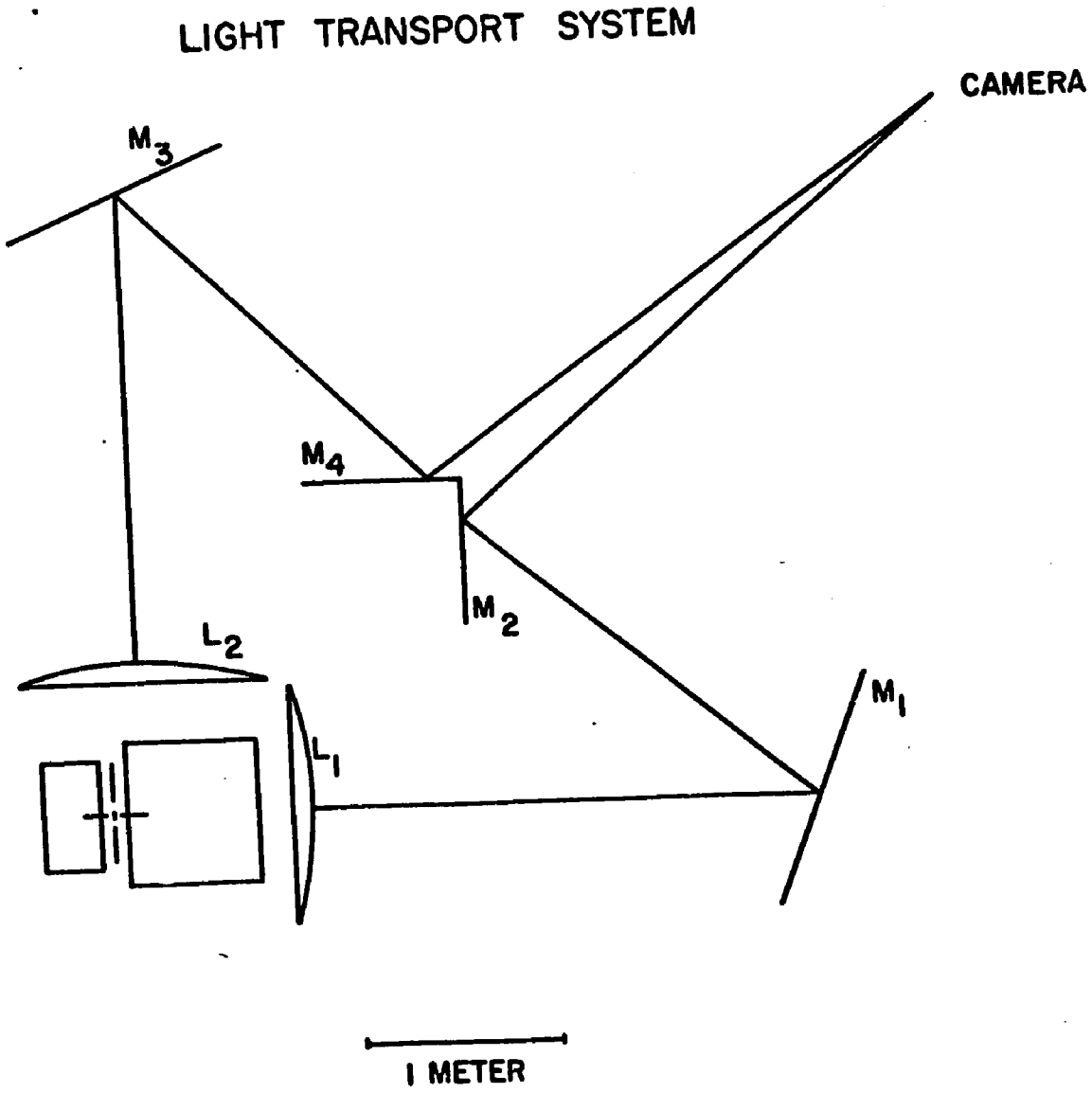



Fig. 11. Optical system looking downstream.

During the course of the experiment several tests for distortion in the optical system were carried out. To test for possible parallax corrections, $\frac{1}{32}$ inch diameter strings were placed at various depths within the experimental area. Corresponding pairs of strings were then aligned parallel in both the top and side views by means of a transit. The strings were then photographed through the optical system. The possible shifts in the position of objects caused by not viewing the chambers normally were found to be less than 0.1 degrees.

Grids consisting of lines spaced one inch apart were placed over the active area of the spark chambers and photographed. Deviations were found to be of the order of one percent over both the one inch spacing of the grid lines and over distances corresponding to the dimensions of the spark chambers.

## E. CALIBRATION RUNS

At the beginning of the experiment a $K^+$ excitation curve showing the number of $K^+$ particles produced as a function of incident beam momentum was obtained. The curve is shown in Figure 12. As the incident pion momentum is lowered, and consequently also the energy available in the center of mass, the number of kaons produced is reduced. As the beam momentum is raised, the $K^+$ yield is increased both because of the increased cross-section for lambda

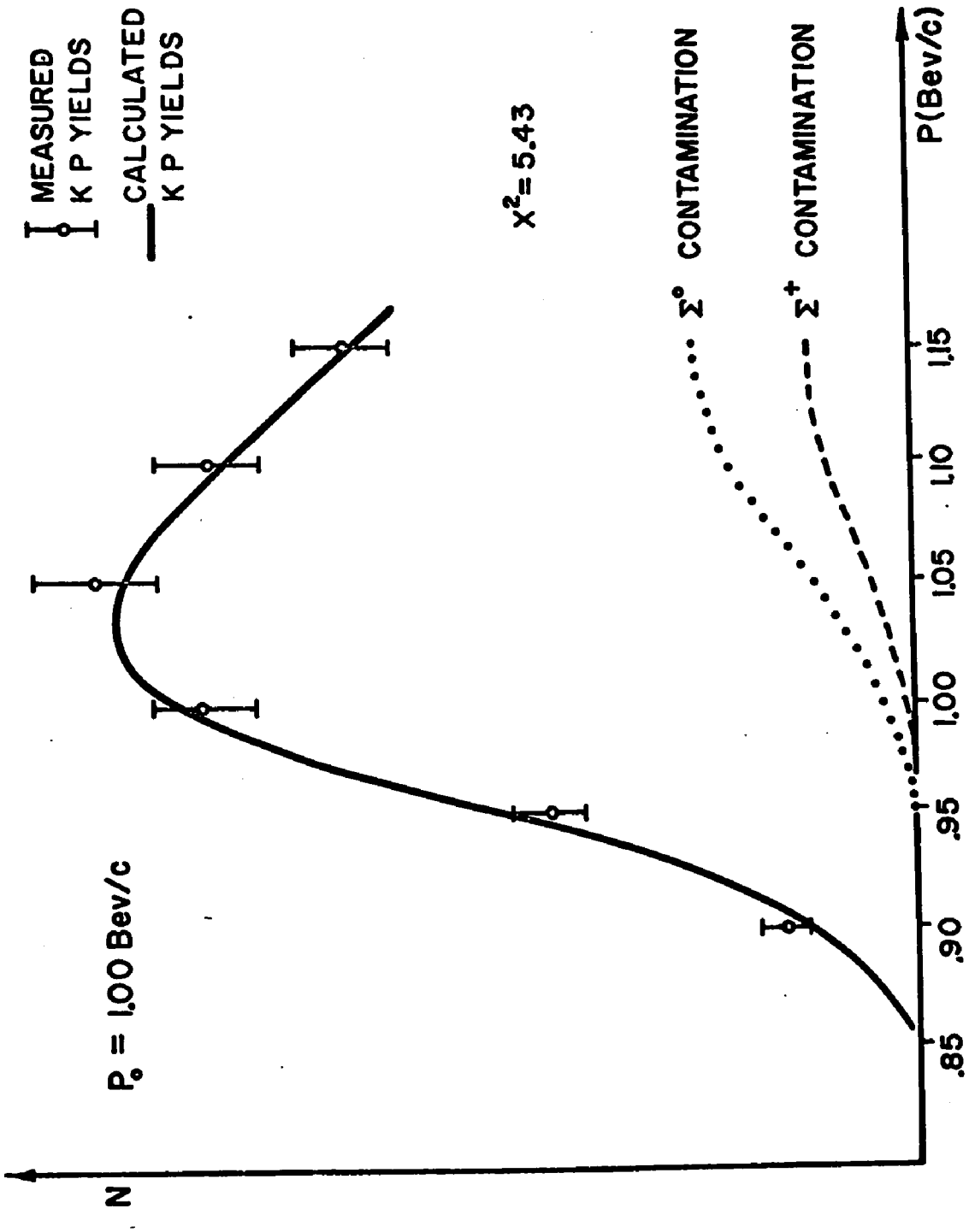



Fig. 12. $K^+$ excitation curve.

production and because of the associated production of kaons with sigma hyperons in the reactions,

$$\pi^+ + n \rightarrow \Sigma^o + K^+$$

$$\pi^+ + p \rightarrow \Sigma^+ + K^+ .$$

For a target nucleon at rest the threshold for lambda production is 896 MeV/c; for the sigma hyperons it is 1030 MeV/c. These thresholds are reduced, however, when the Fermi motion of the neutron or proton in deuterium is considered. From the known production cross-sections, the estimated efficiency of the K-telescope, and the Fermi momentum distribution, a $K^+$ yield curve can be calculated. My collaborator, S. Olsen[16], of the Wisconsin Group has performed such a calculation. The results are also shown in Figure 12. The hyperon composition of the sample was computed to consist of 90% lambdas, 6% neutral sigmas, and 4% charged sigmas.

At the end of the experiment the target was filled with liquid hydrogen and a series of proton-proton elastic scattering runs were made. The 1.0 GeV/c incident protons arrived 100 nanoseconds after they were produced inside the machine. The coincidence requirement was adjusted so that only particles arriving in this time slot could trigger the apparatus. Proton-proton elastic scattering is a pure two-body reaction. Knowing the direction of the incident beam, the angles of

the scattered proton tracks, and the momentum of one of the protons completely determines the event.

A test of the coplanarity of the two out-going proton tracks is shown in Figure 13. The graph is centered at 180.0 degrees and has a full-width-at-half-maximum (FWHM) of five degrees. Knowing the opening angle of one of the proton tracks with respect to the beam line allows one to predict the opening angle of the other proton. Figure 14 shows a plot of the difference of the predicted and measured angles. The curve centers at zero degrees and has a FWHM of three degrees. The fact that these curves are centered at 180.0 degrees and 0 degrees respectively, indicate that the detection apparatus contained no up/down bias.

A plot of the target intersection points of the two proton tracks in horizontal and vertical directions is shown in Figures 15 and 16. The horizontal curve is centered at zero, but the vertical curve is displaced a few tenths of an inch upward in agreement with the beam picture results.

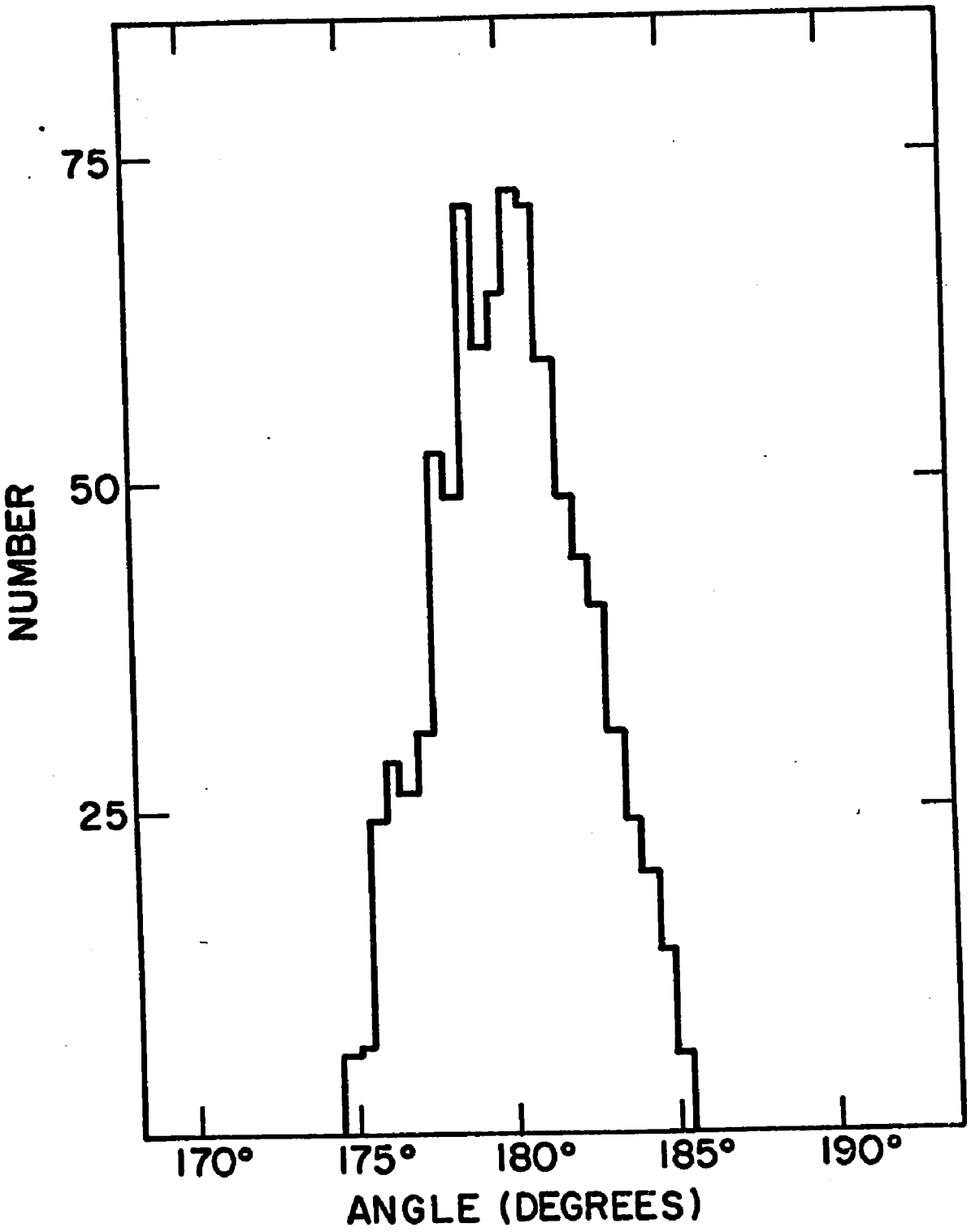



Fig. 13. Proton-proton coplanarity distribution.

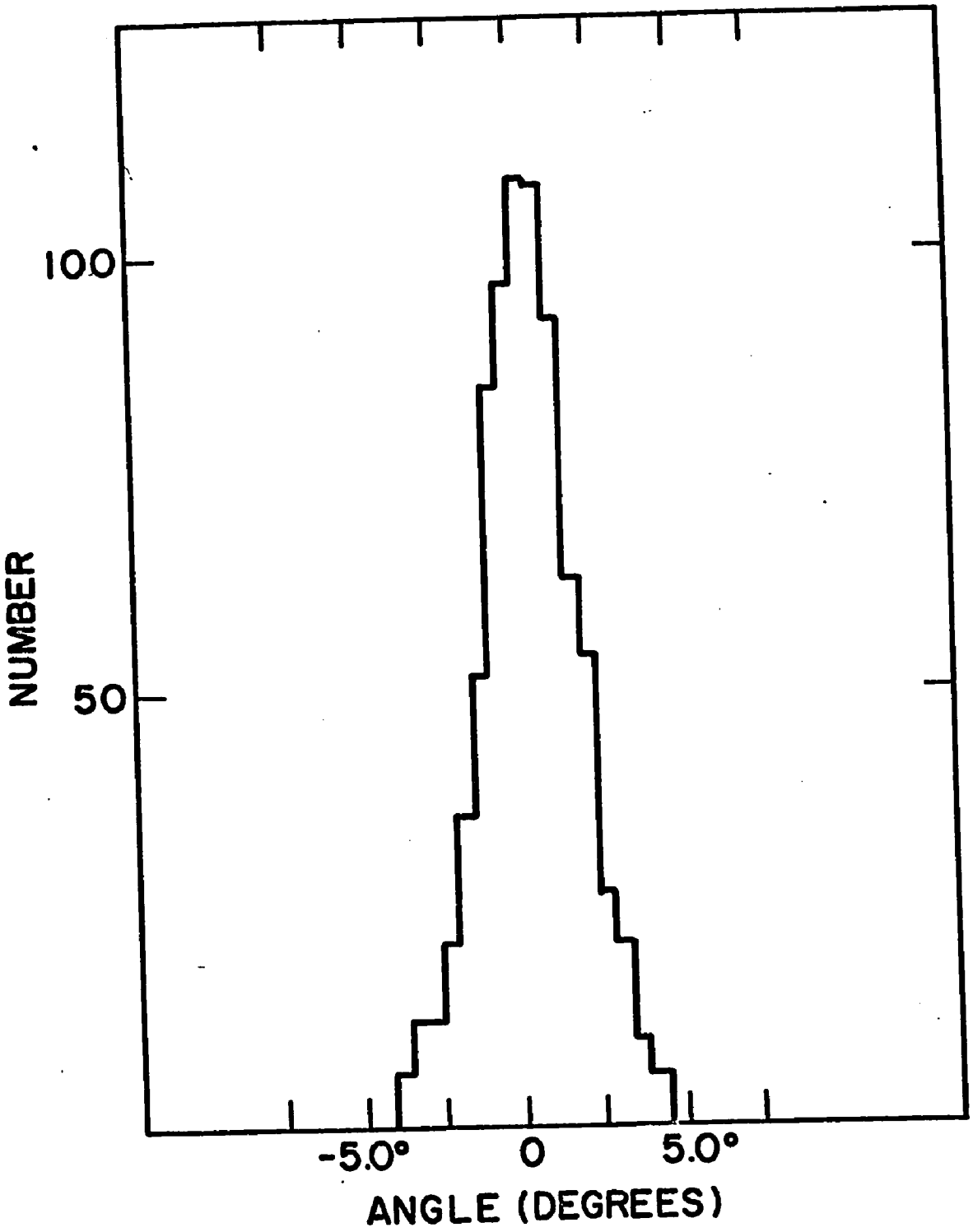



Fig. 14. Proton-proton theta difference distribution.

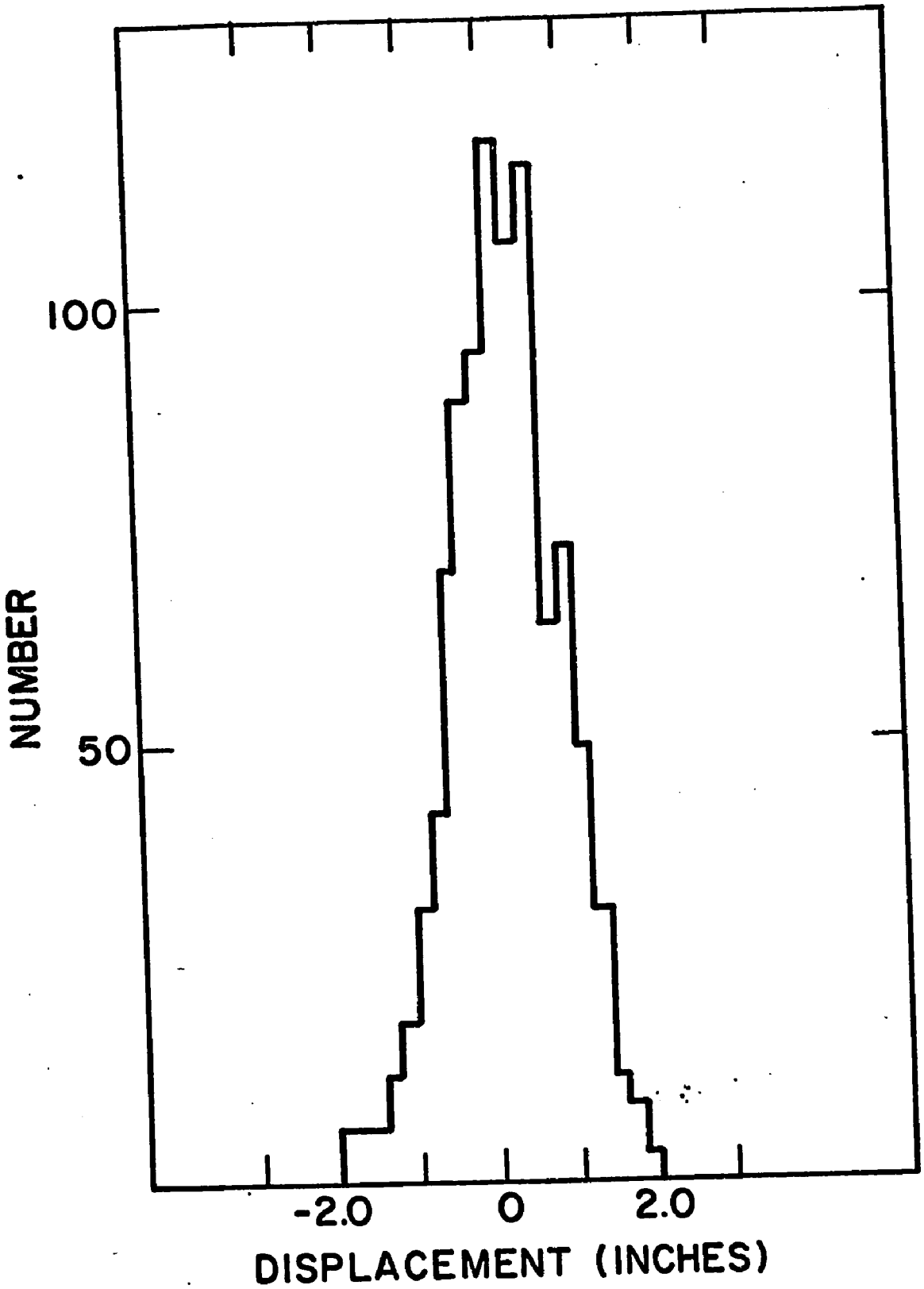



Fig. 15. Proton-proton vertical target intersection distribution.

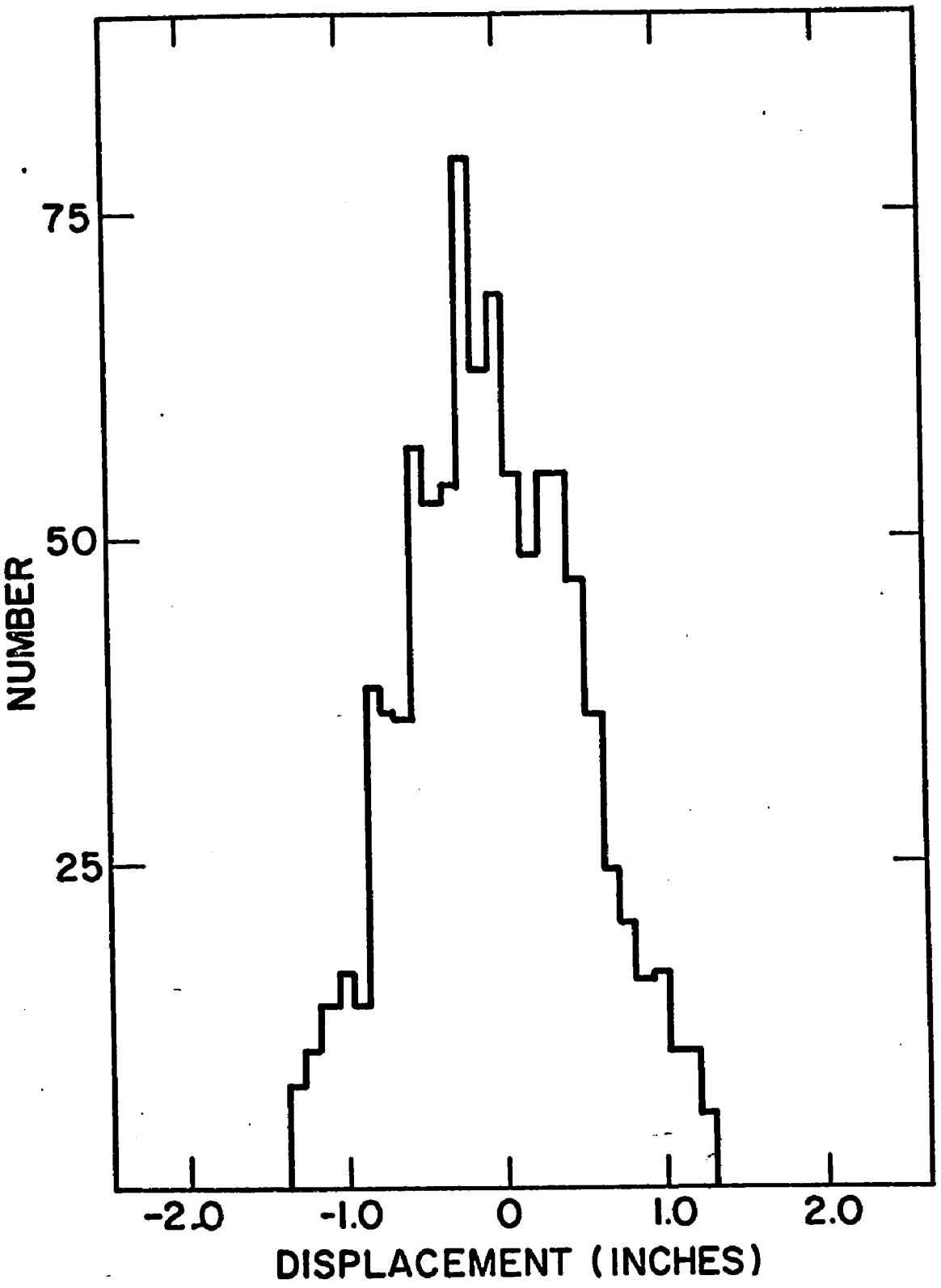



Fig. 16. Proton-proton horizontal target intersection distribution.

# IV. DATA REDUCTION AND ANALYSIS

The total exposure of the film taken during the course of the experiment was approximately 350,000 pictures. Two thirds of the data were taken by triggering on the neutral decay mode and one third by pulsing the chambers on the charged decay mode. All the film was scanned automatically by a flying-spot digitizer. In addition, approximately one third of the film was measured on the mechanical digitizing machines at the University of Wisconsin for comparison. Sections A and B are concerned with this aspect of the data reduction. The kinematical analysis of the events is discussed in Section C. Section D discusses the various consistency checks that were made on the data and possible background reactions.

## A. MASS SCANNING SYSTEM

Our spark chamber film was measured on the Michigan Automatic Scanning System (MASS). MASS consists of a group of programs written for a DDP-124 computer with magnetic tape drive, disc, and a high-precision scanner. MASS was designed for 35 mm transparent film and is essentially a programmed spot scanner. A slightly earlier version of this system is described in the article by Saulys, Meyer, and Allen appearing in Nuclear Instruments and Methods.[17]

Under control of a special in-core calibration table,

MASS examines points only along the centers of the spark chamber gaps. If MASS finds an object within the search pattern, it proceeds to check the object's dimensions and only outputs objects whose sizes are within a certain preset tolerance. The search pattern, the tolerance, and the sizes are all under the control of the calibration table. Thus, this table is essentially a digital map of the film to be scanned.

A grid consisting of 4096 x 4096 points is projected onto a standard (1 inch x $1\frac{1}{2}$ inch) 35 mm frame such that each point is approximately 0.4 mils or 10 microns on the film. Since the demagnification factor of our film is 60, this means we had the capability of resolving the location of objects to within 24 mils in real space.

The automatic scanner has been electronically adjusted to correct for pincushion distortion in the cathode ray tube. To check the optical distortion introduced by the scanning system, several frames containing grids with known spacings were inserted into the film transport mechanism and measured. Deviations were found to be on the one percent level over both small regions of the film, i.e., one inch in real space, and over dimensions comparable to the sizes of our spark chambers.

In addition to scanning spark chamber film completely automatically, a provision exists for interacting with the computer via a light pen as it scans the film frame by frame. An operator can accept or reject a frame, eliminate spurious

sparks, and select a correct track from among other tracks in the chamber all before any information is placed on the output tape. Our charged film generally contained clean events, i.e. few multiple tracks or noise sparks occurred, and was scanned automatically. It required one and a half hours to scan a charged roll containing 3200 frames.

The neutral film was more complicated than the charged rolls. In particular, gamma rays from the decaying pi-zero meson from the decaying lambda frequently entered the chamber and converted into an electron-positron pair. In order to help insure against digitizing these pairs and interpreting them as a neutron event, the light pen mode was employed in scanning the film. It required four to six hours to scan a neutral roll of 3200 frames. The track reconstruction program was much simpler, however, than the one used for the charged data and fewer events had to be initially processed through this program.

A photograph of a neutral event is shown in Figure 17, and the event is further illustrated in Figure 18. The large square figures are scanning fiducials used by MASS while the small cross-hairs near them were used by the hand measurers. Similarly the binary coded decimal lights were used by the computer while the hand measurers recorded the decimal information.

In the top view the beam passes between the $K^+$ and neutron spark chambers. The beam appears to pass through the two chambers along the central axis in the side view.

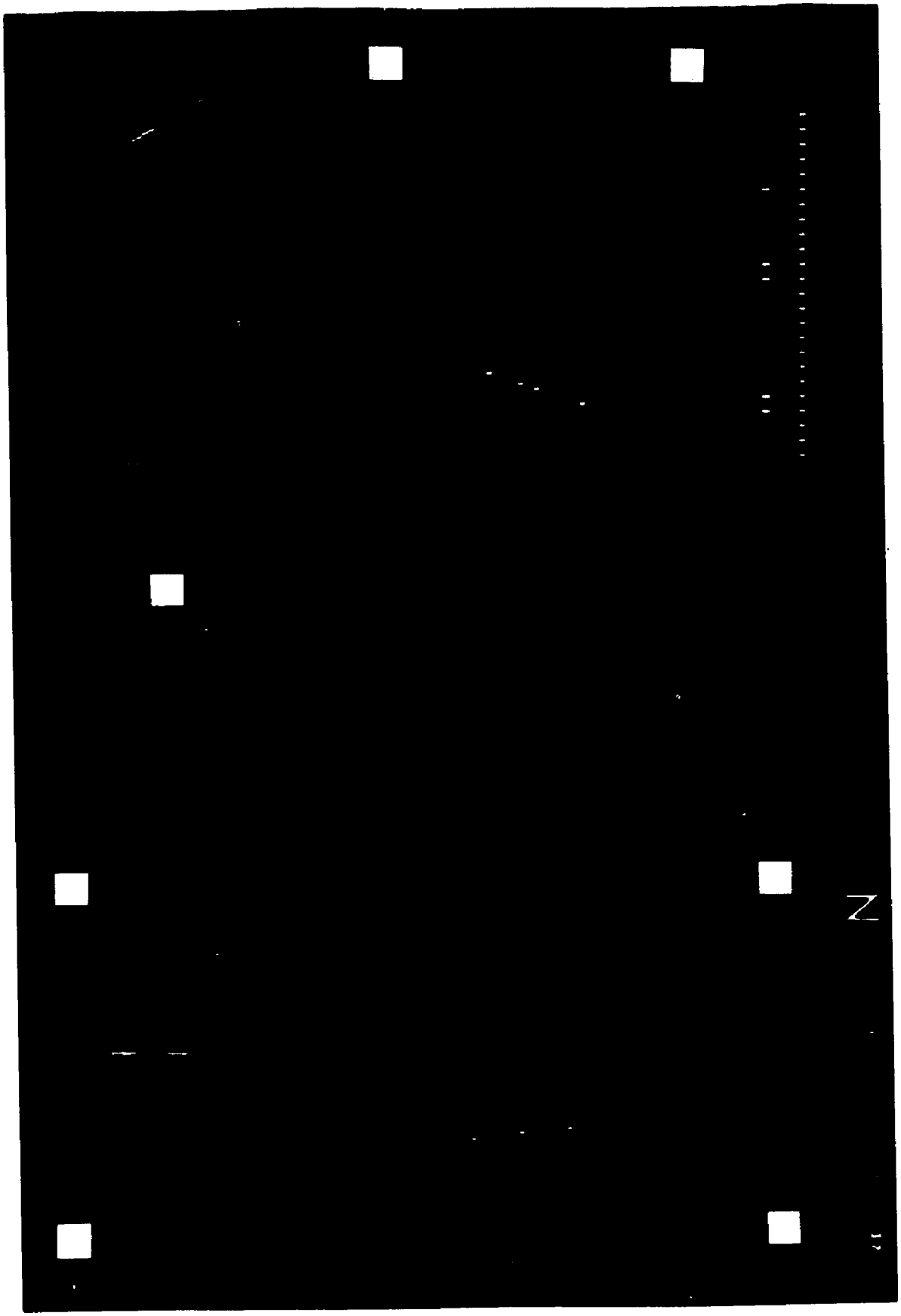


Fig. 17. Neutron event.

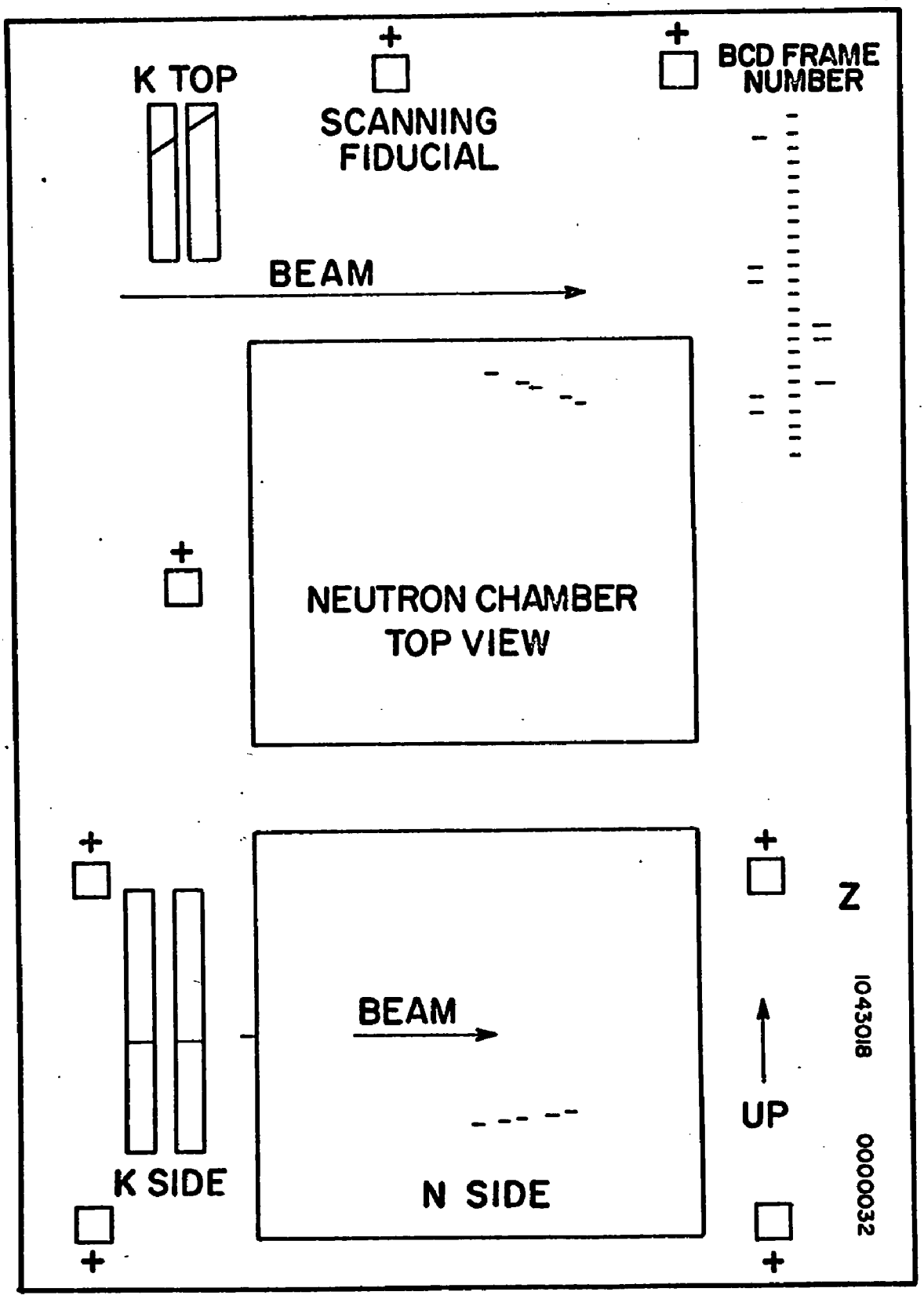



Fig. 18. Schematic of neutron event.

A $K^+$ track and recoil proton track appear in the chamber. The incident neutral particle, of course, must be inferred. A description of the reconstruction of the event is given in a later section.

A photograph of a gamma-ray conversion is given in Figure 19. The multiple scattering of the electron-positron pair is quite evident and typical. The rms scattering angle for pairs was greater than five degrees per $gm/cm^2$ of polyethylene. It was quite easy for the scanner to use the light pen to reject these types of events.

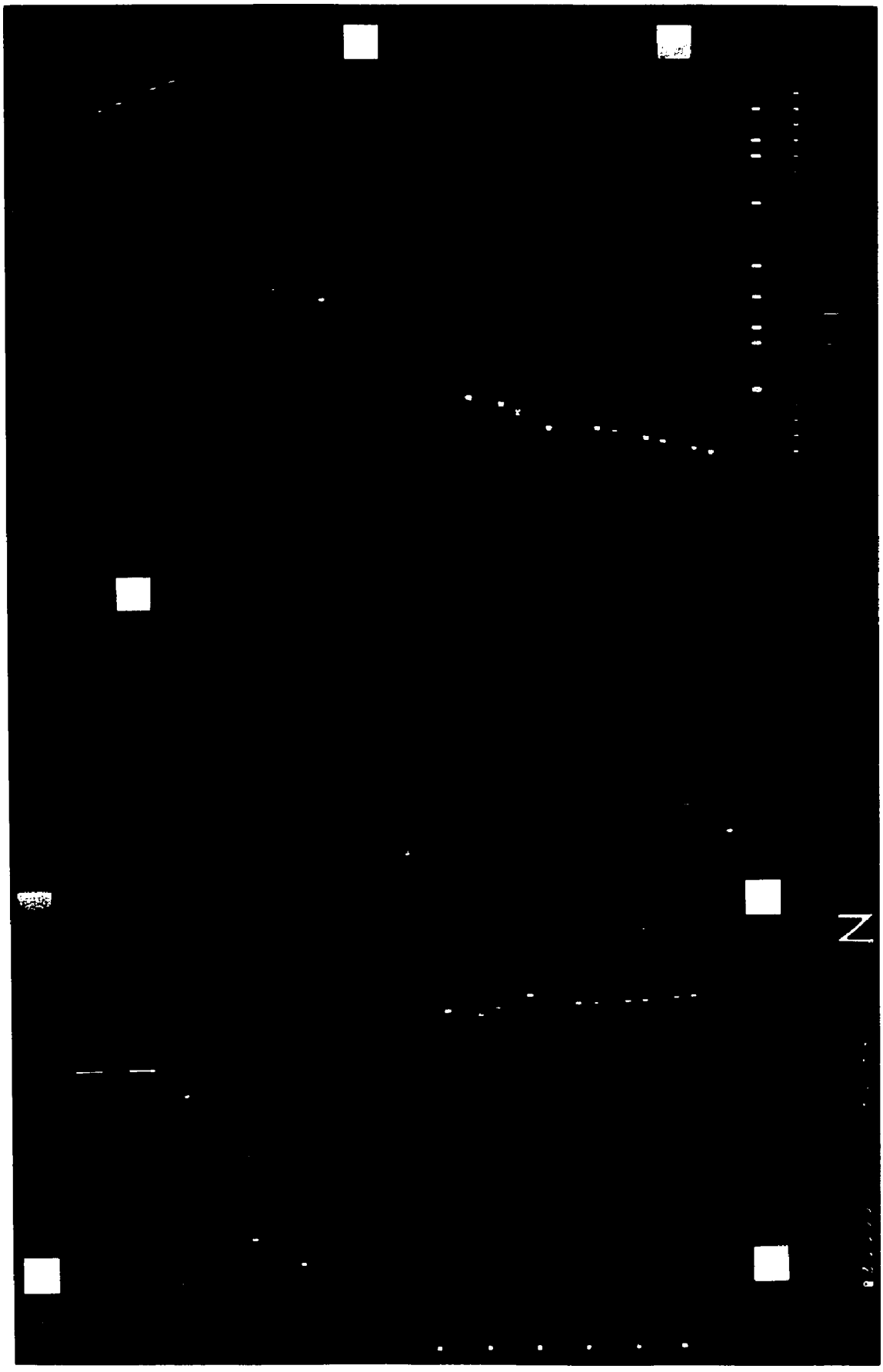



Fig. 19. Gamma-ray conversion.

## B. TRACK RECONSTRUCTION PROGRAMS

The output of the automatic scanner consisted of a magnetic tape containing (x,y) coordinates of the centers of all fiducials and sparks found. In addition to the usual noise sparks encountered in spark chamber film, the scanner would occasionally interpret scratches or dust on the film as a spark. The scanner output tape was processed on an IBM 360 Model 67 computer by the programs described below. The output of these programs was a magnetic tape of reduced data containing the top and side view orthogonal angles of the kaon and proton tracks, the coordinates of the first and last spark of each track in real space, and the apparent target intersection point of the two tracks in the top view.

The basic operation of the charged and neutral track-finding programs was the same. Each spark in a view served as the vertex of a search cone whose dimensions were determined by kinematical constraints. All possible combinations of the sparks in the cone for forming straight lines were attempted. When a series of sparks were least squares fitted to a track, each spark was checked to see if it was within a certain distance of the fitted line. This tolerance was 0.064 inches for a kaon track and 0.144 inches for a proton track. If any spark was found to lie outside this tolerance, it was rejected and a new fit attempted with the remaining sparks. Whenever an acceptable track was found, it was removed from any further consideration in forming new tracks. An acceptable

kaon track had to contain at least four sparks. A proton track had to contain at least three sparks.

When all possible combinations had been attempted for the given cone and any tracks constructed removed, a new cone was formed about the next spark in the view. This process was repeated until all the sparks in the given view were exhausted.

The principal difference between the charged and neutral reduction programs was that the charged routines contained some further decision-making logic to handle the possibility of multiple tracks occurring in the chambers. Only those events were accepted for which all except one of the multiple tracks in each chamber were eliminated.

The efficiency of MASS for retrieving charged events upon a remeasurement of a roll was 90% or better and all angles were found to be reproducible to within $\pm$ 0.5 degrees. This was also approximately the scanning efficiency of MASS in comparison with the events measured at the University of Wisconsin. Ten percent of the charged film was found to satisfy the kinematical limitations described in the next section and formed the "good events" category used in the final analysis.

The scanning efficiency for the retrieval of neutral events upon remeasurement was 85%. The scanning efficiency of MASS in comparison with the events mechanically measured at the University of Wisconsin was also approximately 85%. MASS lost those events which either underwent an additional

scattering with the H in the plates or multiple-scattered appreciably. Approximately 2-3% of the neutral film was found to satisfy the kinematical requirements and formed the "good events" category used in later analysis.

## C. KINEMATICAL ANALYSIS

Each event on the reduced data tape generated by the track reconstruction program was processed by the analysis program described below. Since the target neutrons in the deuterium possessed a distribution of energies assumed to be given by the Hulthen distribution[18], an exact reconstruction of the events could not be carried out. Instead, a quasi-reconstruction of the events was made which selected a sample of lambdas free from contamination. In addition, there was no up-down bias in the selection criteria and the cos $\omega$ curves were determined from measured quantities and did not depend heavily on the method of analysis employed.

The charged and neutral data were analyzed with the same analysis program. That is, even the charged proton tracks were treated as proton recoils. Both the charged and neutral events had to be at least three sparks long, appear to originate in the deuterium target, and the first and last sparks of the tracks had to remain within a fiducial volume which contained a one inch zone surrounding the neutron chamber. A charged track had to start in gap one or two, while a neutron track could not begin earlier than gap three, thus

insuring against veto failures in the anti-counter, $\bar{P}$.

Figure 20 illustrates the salient features of the analysis method. Two-body kinematics were used in the production process. Initially the target neutron was assumed to be at rest. The measured $K^+$ direction, the nominal beam direction as determined from the calibration runs discussed earlier, and the beam momentum, determined the direction and momentum of the lambda. The kaon track was extrapolated back to the nominal beam line and the lambda was assumed to originate from the intersection point. The lambda was then allowed to travel a distance according to its mean lifetime, typically two inches, and the proton or neutron track inferred by connecting this end-point with the apparent conversion point in the polyethylene plate. Using the direction of the inferred baryon and the lambda, an opening angle between the baryon and lambda was determined. The opening angle determined in this manner was called the "measured angle".

The decay baryon was assumed to have undergone a free n-p or p-p scattering with the hydrogen atoms in the polyethylene. From the inferred n-p or p-p scattering angle together with the energy of the recoil calculated from range measurements in the polyethylene, the energy of the decay baryon was determined. This energy was then used to calculate an opening angle with the hyperon, called the "calculated angle", which was compared with the measured angle. An agreement of four degrees was required for an event to be used in the later analysis.

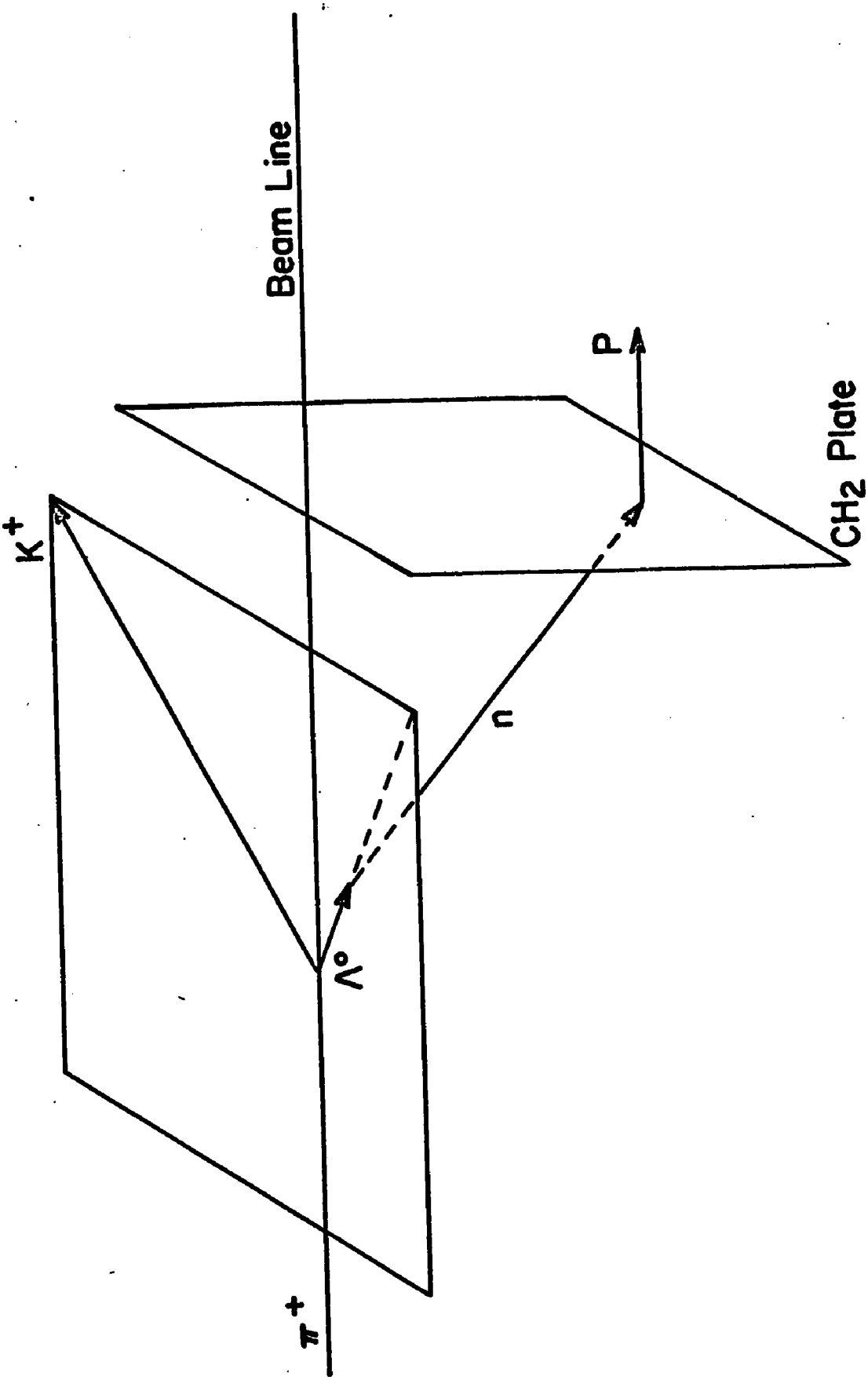



Fig. 20. Reconstruction of an event.

A reconstruction of the event was performed for five momentum values for the target neutron (0, $\pm$ 25 MeV/c, and $\pm$ 50 MeV/c along the incident $\pi^+$ direction) and the angle between the decay neutron and the $\Lambda^o$-hyperon in the laboratory predicted by each fit was compared with the measured angle. The first value of the target momentum which yielded a difference in angles of $|\Delta\Theta| < 4^o$ stopped the calculation, and the event was accepted. If none of the five target momenta satisfied this criterion, the event was rejected.

In this manner, 4762 neutral events and 8506 charged events were selected for later analysis. The lambda center of mass production angles for both the neutral and the charged data are shown in Figure 21. Backward going lambdas in the center of mass were primarily chosen. The two distributions are very similar, and hence, also the polarization of the lambdas in the two samples. The data were analyzed, as explained later, however, in such a way as to correct for possible differences.

The neutron-proton scattering angles are shown in Figure 22. The neutral mode has angles between zero and forty-five degrees. The angle range for the charged data is between zero and ten degrees. In fact, of course, all the angles for the charged data should have been zero degrees, but uncertainties in the lambda direction and travel before decay smeared the angles into larger values.

The distributions of the decay angles for the protons and neutrons in the lambda rest frame are shown in Figures

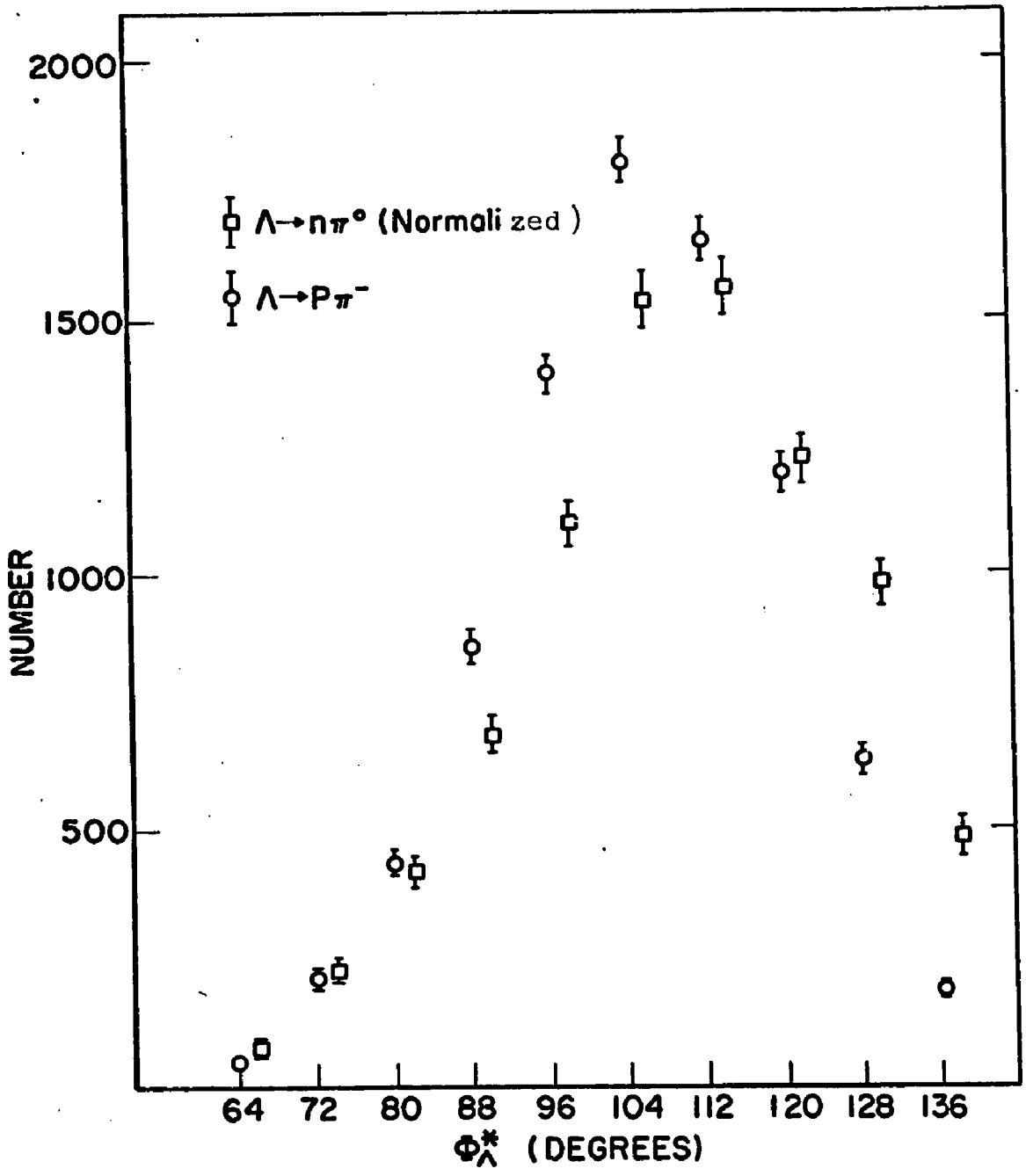



Fig. 21. Lambda center of mass production angle distributions.

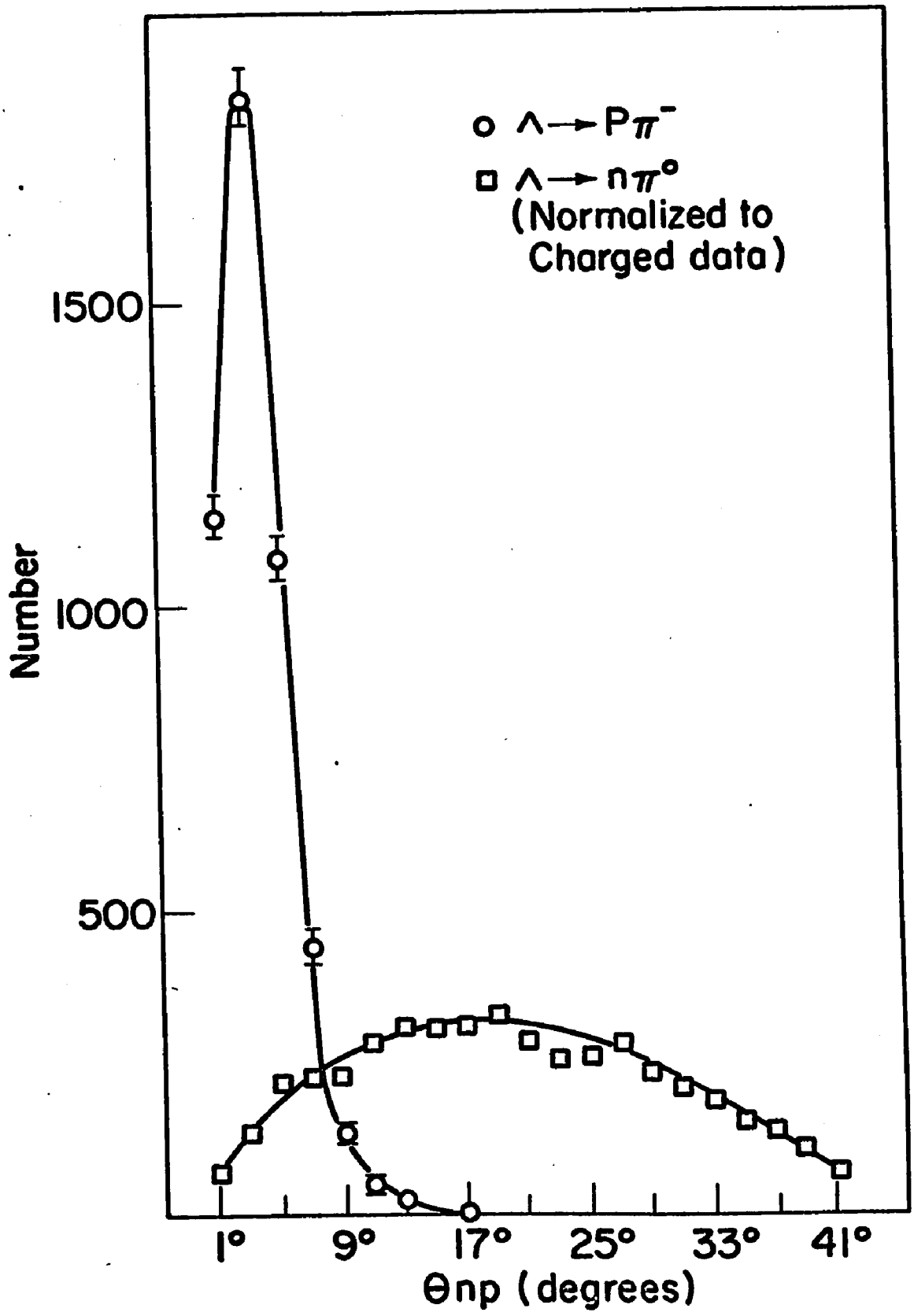



Fig. 22. Neutron-proton scattering angle distributions.

23 and 24. Differences in the two distributions arise mainly because of the different energy detection efficiencies for the two different modes. The neutron detector favored lower energies, whereas the corresponding protons tended to stop in the deuterium target.

For each event passing the reconstruction criteria, the Lorentz-invariant quantity,

$$\cos \omega = \frac{\vec{p} \cdot \hat{v}}{p^*}$$

was calculated, where p is the laboratory momentum of the decay proton or neutron, $p^*$ the momentum in the lambda rest frame, and $\hat{v}$ is the direction of the normal to the production plane,

$$\frac{\vec{\pi} \times \vec{k}}{|\vec{\pi} \times \vec{k}|} .$$

Cos $\omega$ is the angle between the lambda polarization and the decay baryon in the lambda rest frame. The angular distributions of the decay nucleons in the rest frame of the lambda did not follow the usual linear relationship, i. e., $N = \frac{1}{4\pi} (1 + \alpha \overline{P} \cos \omega)$. This was principally caused by the uncertainty in the direction of the lambda polarization due to the Fermi motion of the target neutron, an effect common to both the charged and neutral data. Deviations from linearity could also be caused by energy dependent detection efficiencies, by errors in the neutron momentum because it recoiled off C

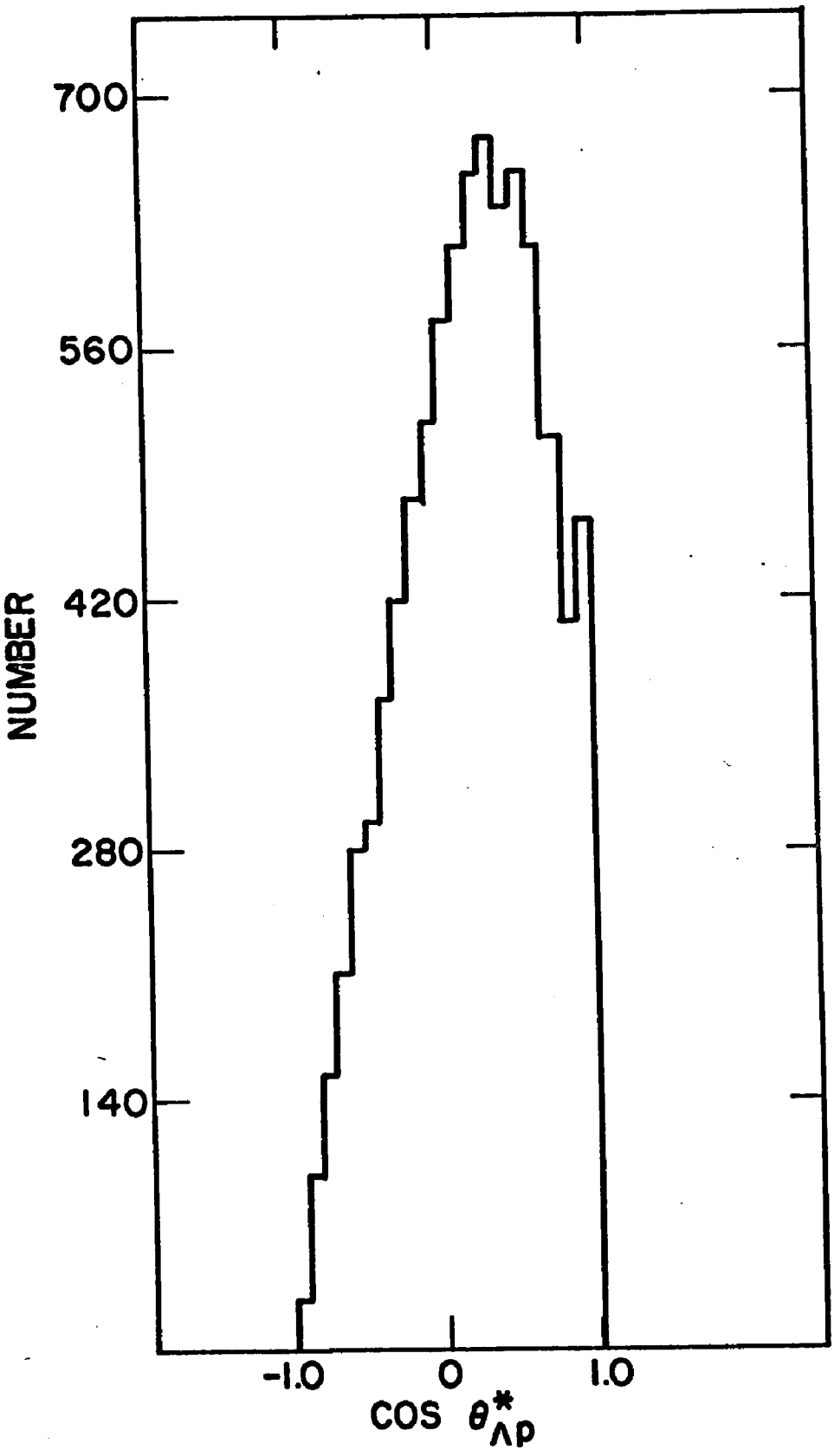



Fig. 23. Lambda-proton decay angle distribution.

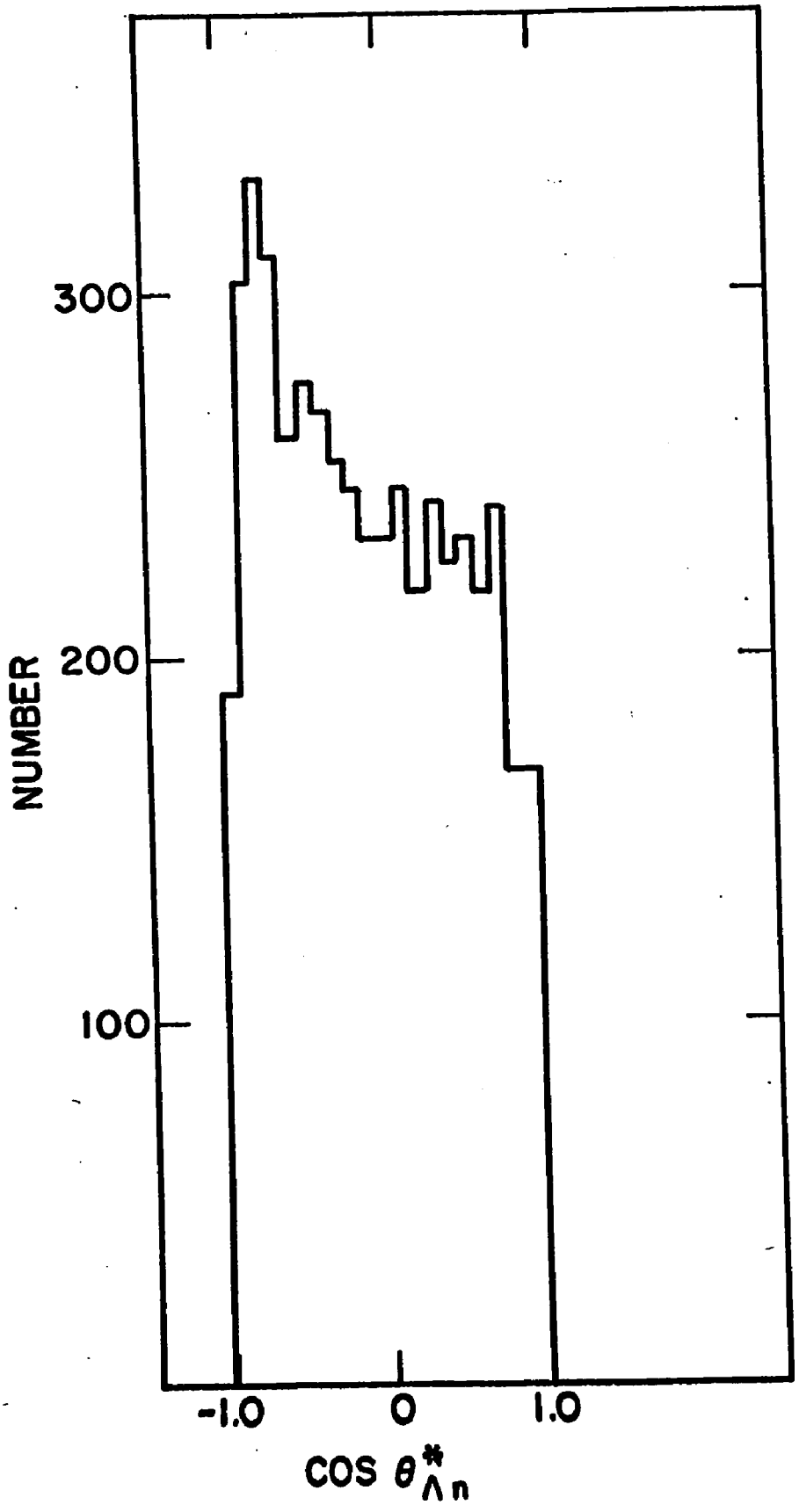



Fig. 24. Lambda-neutron decay angle distribution.

rather than H in the polyethylene plates, and by geometric limitations in the solid angle subtended by the chamber. In addition, the ratio $p/p^* \sim 0.6$ for a typical event, so that these uncertainties in $\vec{p}\cdot\hat{v}$ were amplified in calculating cos $\omega$.

These effects could depend on the magnitude of cos $\omega$ but should not depend on its sign. To check this later assertion, distributions were made for baryon energy as a function of positive and negative cos $\omega$. The distributions of energy for the charged and neutral modes are given in Figure 25. The neutral data have a $\chi^2 = 8.3$ for 9 degrees of freedom. The charged data have a $\chi^2 = 11.3$ for 8 degrees of freedom.

From the distributions of the data as a function of cos $\omega$, the product of the asymmetry parameter times the average hyperon polarization of the sample, $\alpha\overline{P}$, can be determined in the manner indicated below. If the average hyperon polarization were the same for both the neutral and charged data, then $\alpha_o\overline{P} / \alpha_-\overline{P}$ would also equal $\alpha_o / \alpha_-$. To correct for the possibility of different hyperon polarizations in the samples, the data were divided into seven different lambda center of mass production angle bins, and for each bin the ratio $\alpha_o\overline{P}/ \alpha_-\overline{P} = \alpha_o/\alpha_-$ was formed. These seven ratios were then statistically averaged to yield the ratio $\alpha_o / \alpha_-$ for the total sample.

The product of the charged asymmetry parameter times the average hyperon polarization as a function of lambda

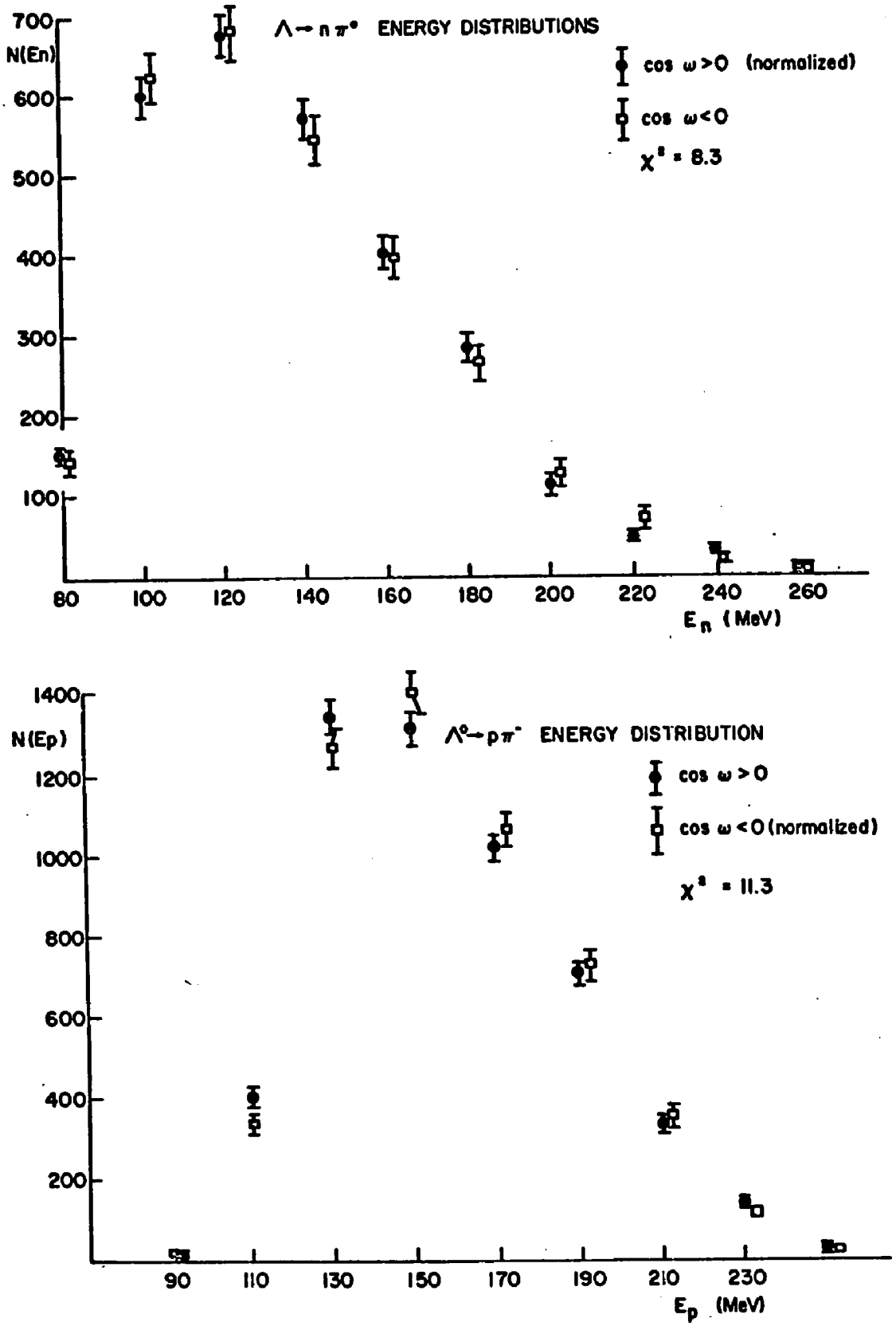



Fig. 25. Energy distributions for positive and negative cos ω values.

production angle is shown in Figure 26. For comparison, the recent results of Cleland, et al.[19] have also been plotted. Cleland used a 1030 MeV/c beam rather than 1000 MeV/c as in our experiment and the beam particles were incident on a liquid hydrogen target rather than deuterium. The curves have approximately the same shape and both curves show that the polarization was not a strong function of production angle.

The distributions in cos $\omega$ for the complete samples of the neutral and charged data for all production angles are shown in Figure 27. The neutral distribution has been normalized to the total number of proton events for comparison. The curves extend beyond cos $\omega$ = +1.0 and cos $\omega$ = -1.0 because of the uncertainties in the neutron or proton momentum and direction. A Monte Carlo curve has also been plotted for each decay mode. The Monte Carlo curves were calculated assuming an $\alpha\overline{P}$ of 0.60 for both decays. As discussed above, the data were actually first divided into lambda center of mass production angle bins, and then for each production angle bin, a distribution in cos $\omega$ was obtained. The curves of Figure 27 are useful, however, in discussing the method employed to determine $\alpha\overline{P}$ from the cos $\omega$ curve.

In order to compare the asymmetries for the two cos $\omega$ curves in such a way as to cancel the effect of those distortions which depend on the magnitude of cos $\omega$ but not on its sign, a parameter $\epsilon$ was defined for each pair of bins with the same value of $|\cos \omega|$ as follows:

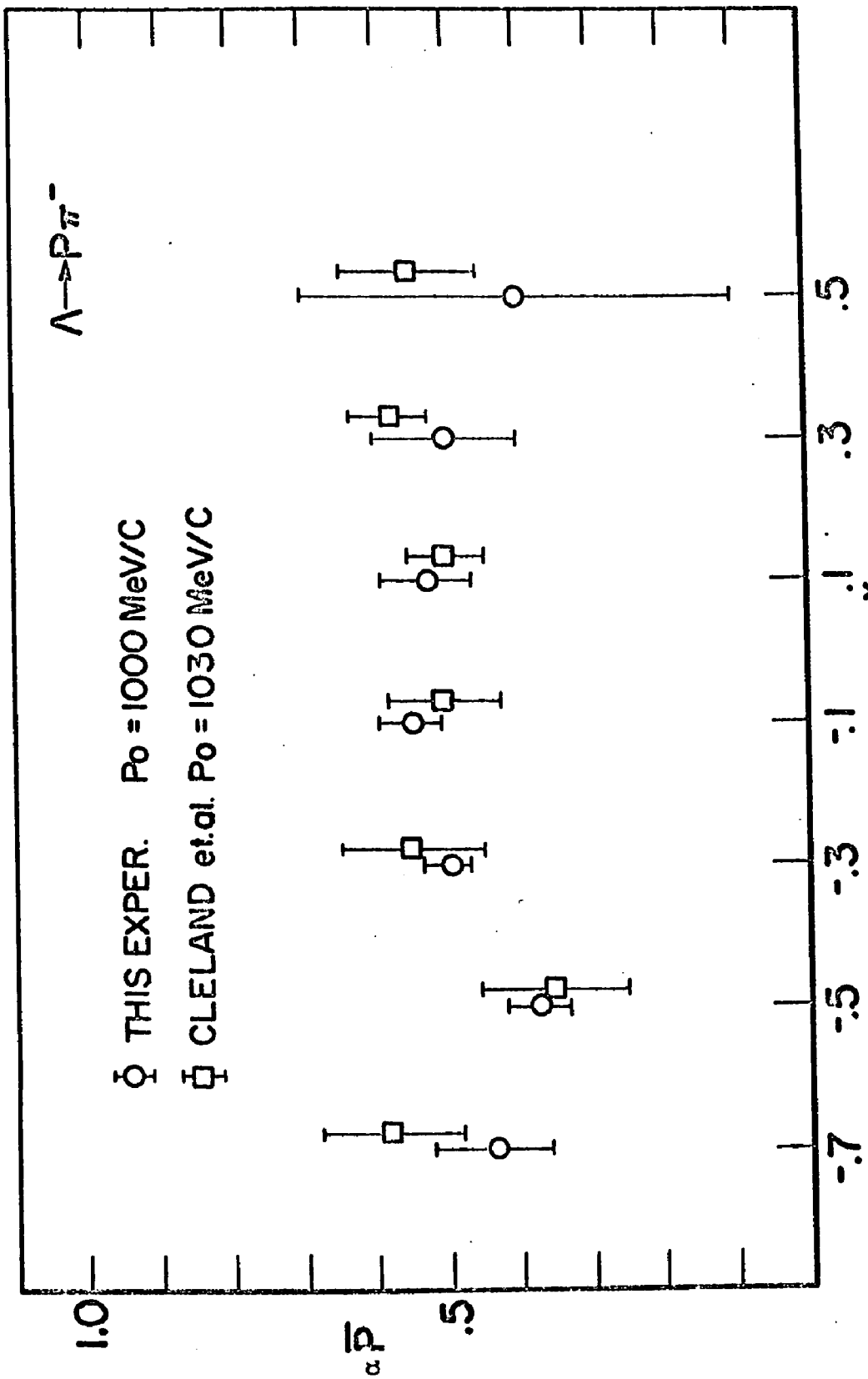



Fig. 26. Charged asymmetry parameter as a function of lambda production angle.

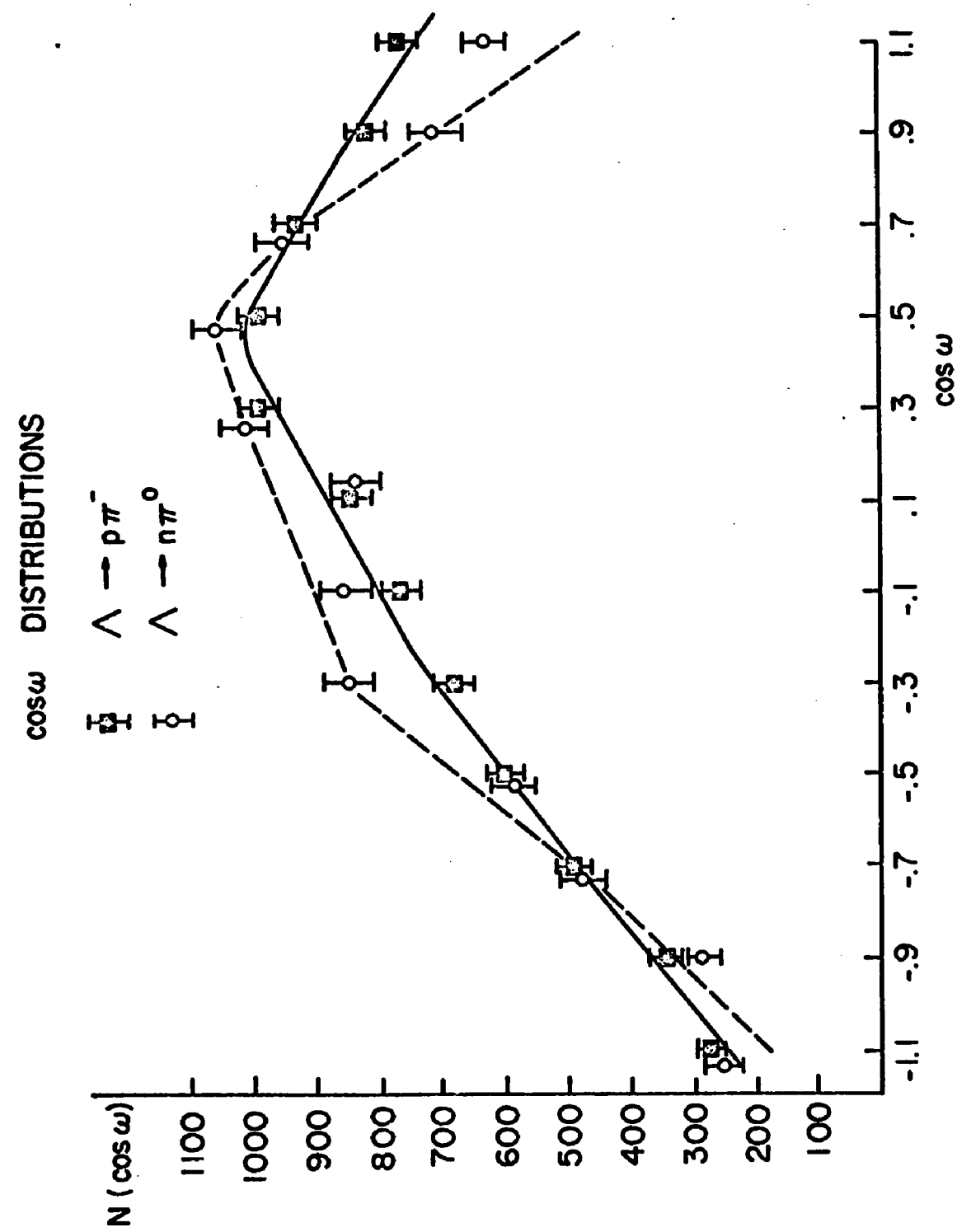



Fig. 27. Cos w curves for charged and neutral data together with Monte Carlo predictions.

$$\epsilon = \frac{N^+ - N^-}{N^+ + N^-} \quad x \quad \frac{1}{|\cos \omega|}$$

where $N^+ = N(+|\cos \omega|)$ and $N^- = N(-|\cos \omega|)$. Each pair of bins was assigned an error, $\delta_\epsilon = (N^+ + N^-)^{-\frac{1}{2}} \quad x \quad \frac{1}{|\cos \omega|}$.

Then the weighted average of the $\epsilon$ values was calculated to obtain the best value for the entire curve. In the absence of distortions the quantity $\epsilon$ defined above equals $\alpha\bar{P}$ for each value of $|\cos \omega|$. The Monte Carlo calculations predict, to within an accuracy of 3%, that if $\alpha_o / \alpha_- = 1$, then the asymmetry ratio $\epsilon_o/\epsilon_-$ should also equal one.

The parameters $\epsilon$ defined above for the charged and neutral data of Figure 27 are given in Table III and do not change outside of statistical fluctuation for the various values of $|\cos \omega|$. This consideration combined with the similarity between the proton and neutron points in Figure 27 support the Monte Carlo conclusion.

In order to arrive at the selection criteria of $|\Delta\Theta| \leq 4.0$ degrees for an event to be acceptable, the timing distributions of the $K^+$ lifetime for the charged and neutral data were examined. The curves were examined for relative prompt contamination by normalizing the curves for times greater than one kaon lifetime, and then seeing how well the curves fit at earlier or prompt times. Prompts were caused primarily by failures in the water anti-Cherenkov counter, $\bar{K}_2$, discussed earlier, which failed to veto pion-nucleon elastic scatters. That is, the prompts were mainly due to strong interactions

TABLE III

ASYMMETRY PARAMETERS AS A FUNCTION OF $|\cos w|$

FOR NEUTRAL AND CHARGED DATA

| $\lvert\cos w\rvert$ | $\epsilon_o \overline{P}$ | $\delta_o$ | $\epsilon_- \overline{P}$ | $\delta_-$ |
|---|---|---|---|---|
| 0.9 | 0.475 | 0.034 | 0.489 | 0.024 |
| 0.7 | 0.448 | 0.050 | 0.438 | 0.038 |
| 0.5 | 0.559 | 0.066 | 0.495 | 0.050 |
| 0.3 | 0.272 | 0.103 | 0.602 | 0.081 |
| 0.1 | -0.127 | 0.325 | 0.536 | 0.248 |

$\langle \epsilon_o \overline{P} \rangle = 0.465 \pm 0.025$ $\langle \epsilon_- \overline{P} \rangle = 0.484 \pm 0.018$

and, thus had no up-down asymmetry. Their effect was to reduce $\alpha\bar{P}$ for the contaminated sample. Prompt contamination in the neutral data only, therefore, would show up in the form of a reduced ratio for the neutral to charged asymmetry. A second effect of relative prompt contamination would be a difference in the neutral to charged asymmetry ratio for early kaon lifetimes and late times. There are other possible background contaminations in the data which would not show up in the lifetime curves, but discussion of these is delayed until Section D.

The $K^+$ lifetime distributions for the data used in the analysis discussed above are shown in Figure 28. The relative prompt contamination is estimated to be about 1.0 $\pm$ 1.0% more neutral background than charged. The results of the time early and time late analysis are summarized in Table IV.

TABLE IV

ASYMMETRY RATIOS FOR TIME EARLY AND TIME LATE DATA

| Time Early Data | Time Late Data | All Times |
|---|---|---|
| 1.001 $\pm$ 0.091 | 0.939 $\pm$ 0.094 | 0.977 $\pm$ 0.065 |

The time early data corresponded to events with times less than one $K^+$ lifetime; the time late data data for events with larger times. The values are consistent with no

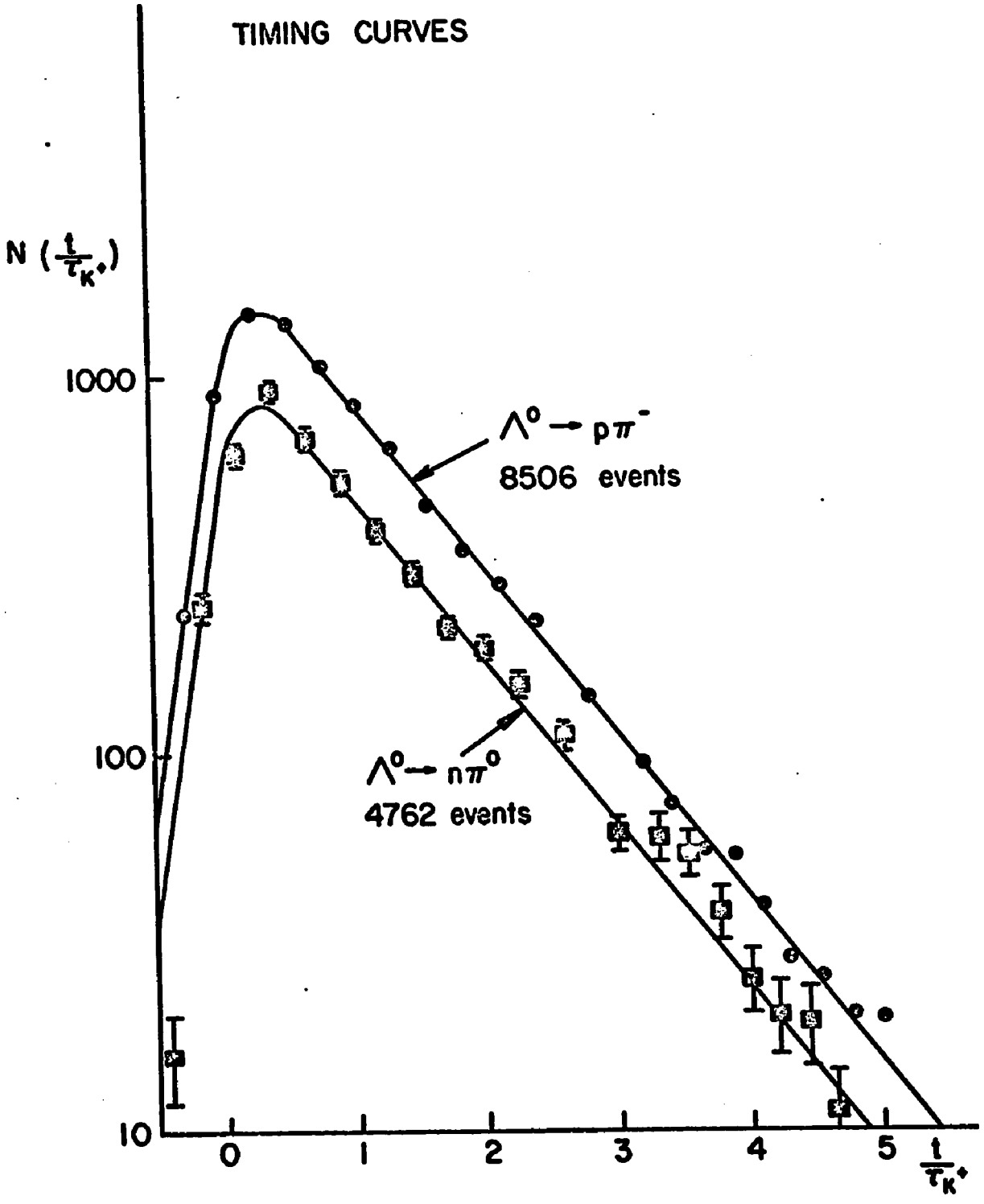



Fig. 28. $K^+$ lifetime distributions for charged and neutral data.

prompt contamination.

When $|\Delta\Theta|$ cuts of 2.0 and 3.0 degrees were made on the data, no significant differences from the results above were obtained. However, when larger angle acceptances were permitted, large prompt contamination set in and differences of 20 to 30% in time early and time late samples arose.

The effect of fiducial volume cuts on the data was also examined. Making three further successive one-half inch cuts on the fiducial volume had no effect on the relative prompt contamination in the timing distributions and did not yield results significantly different from those of Table V.

The possible effect of MASS scanning inefficiencies in retrieving sparks on the neutral and charged asymmetries was examined by calculating $\alpha\overline{P}$ for the decays as a function of spark length. The results are shown in Figure 29. There does not appear to be any difference in the asymmetries for short length tracks versus longer tracks. Similarly, there does not appear to be any significant difference between the neutral and charged data.

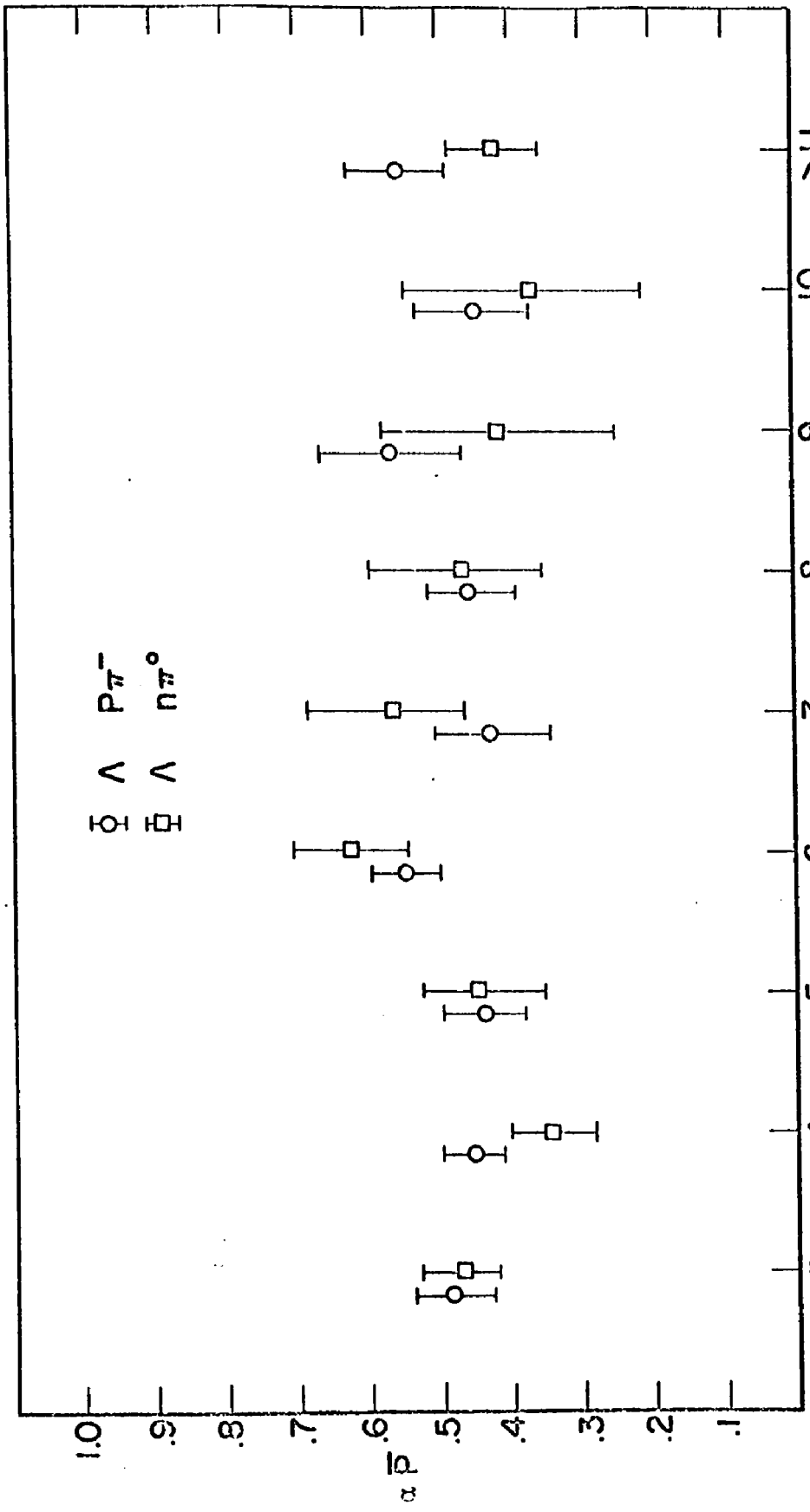



Fig. 29. Asymmetry parameters as a function of spark length.

## D. POSSIBLE BACKGROUND CONTAMINATION

There are four possible sources of background contamination at our beam momentum which would not be evident in the $K^+$ lifetime curves. The possible effect of each type of background on the data and the estimated percentage contamination of each will be discussed in this section.

The first background to be considered is that caused by the production of $\Sigma^o$ hyperons in the reaction, $\pi^+ + n \rightarrow \Sigma^o + K^+$, which is possible because of the reduced energy threshold allowed by the Fermi motion of the target nucleons. The $\Sigma^o$ decays immediately by the electromagnetic decay process, $\Sigma^o \rightarrow \Lambda^o + \gamma$, generating a source of $\Lambda^o$ hyperons whose polarization is less than the sample of lambdas produced directly. If the neutrons from the decay, $\Lambda^o \rightarrow n\pi^o$, are detected with a different efficiency than the protons from the decay, $\Lambda^o \rightarrow p\pi^-$, for the sample of lambdas generated by the $\Sigma^o$ hyperons, then the polarization of the total sample of lambdas for the neutral and charged modes will be different. Thus, in dividing $\epsilon_o \overline{P}$ by $\epsilon_- \overline{P}$, it would be incorrect to cancel the polarization factors, $\overline{P}$.

Monte Carlo calculations have shown that to within ten percent, the neutrons and protons from the $\Sigma^o$ generated lambdas are detected with equal efficiencies. Thus, since the $K^+$ excitation curve mentioned in Chapter II, Section E, shows at most 6% $\Sigma^o$ contamination, there could be at most a 1% difference in the detection of the neutrons versus the protons.

A second possible source of contamination arises from the production of $\Sigma^+$ hyperons in the reaction, $\pi^+ + p \rightarrow K^+ + \Sigma^+$. The $\Sigma^+$ decays primarily via the two modes, $\Sigma^+ \rightarrow p\pi^o$, or $\Sigma^+ \rightarrow n\pi^+$. The first decay is governed by a parity violating parameter equal to -1, while the second reaction appears to conserve parity[10,20]. Since the sigma is produced close to threshold, however, the hyperon probably has a low polarization and there might be no difference in the asymmetries of the protons or neutrons detected in the two modes. Since the decay baryons from $\Sigma^+$ decay havegreater energies than those from lambda decay, they are detected with only 1/4 the efficiency. Thus, the possible effect of $\Sigma^+$ contamination is limited to: 1/4 (detection efficiency) x 4% ( $\Sigma^+$ background estimated from $K^+$ excitation curve), or less than or equal to one percent.

A third source of contamination arises from the possibility of misidentifying negative pi-mesons in the charged decay of the lambda as protons. This is not very likely, however, since the mesons come off both with larger energies and greater opening angles with respect to the lambda hyperons. The effect of this contamination is also estimated to be less than or equal to one percent.

The final and most serious potential source of background arises from the neutral pi-mesons in the decay, $\Lambda^o \rightarrow n\pi^o$. The neutral pi-mesons decay immediately into photons of energy up to 200 MeV which can then materialize as electron-positron pairs which might possibly fake a neutron. The

radiation length of lead placed in front of the neutron assembly cut down the number of photons entering the chamber by 60%. Most of the remaining photons that converted in the chamber, however, gave rise to electron-positron pairs that left the fiducial volume. Requiring the proton recoils to remain in the chamber eliminated all the lepton pairs arising from photons with energy greater than 25 MeV.

An overly pessimistic estimate of the number of photons in the chamber compared to the number of neutrons is 30%. Since the scanning criteria for the neutral data rejected those tracks with more than one prong or those that multiple scattered appreciably, a reasonable estimate of the scanning efficiency for detecting pairs is 90%. Monte Carlo calculations show that the efficiency of a photon for passing the reconstruction criteria is 0.4 times the efficiency for neutrons. Thus, the percentage photon contamination is estimated to be, 0.3( % photons) x 0.1(% scanned) x 0.4 (efficiency for passing selection criteria) = 1.2 %. This is of the same order of magnitude as the possible negative pi-meson contamination in the charged decay mode, and thus, the asymmetries of both decay modes would be diluted by the same amount.

# V. EXPERIMENTAL RESULTS

An asymmetry, $(\alpha\overline{P})_i \pm \delta_i$ , was calculated for both the charged and neutral data for $\cos \Theta^*_\Lambda$ = -0.7, -0.5, -0.3, -0.1, +0.1, +0.3, and +0.5 as explained in the last Chapter. For each center of mass production bin, the ratio,

$$\frac{\alpha_o \overline{P}}{\alpha_- \overline{P}} = \frac{\alpha_o}{\alpha_-}$$

was formed. The error assigned to each ratio was determined from the standard error formula,

$$\Delta = \frac{\alpha_o}{\alpha_-} \times \left[ (\delta_o/\alpha_o)^2 + (\delta_-/\alpha_-)^2 \right]^{\frac{1}{2}}$$

The results are tabulated in Table V . The ratios were then statistically averaged to yield, $\alpha_o/\alpha_- = 0.977 \pm 0.065$. It is interesting to note that if there had been no distortions in the cos $\omega$ curves, the expected error based on 4760 neutron events and 8500 proton events would have been $\pm$ 0.045. The error was then adjusted by folding in a 2% uncertainty for possible early time background and a 2% error to account for possible distortions in the cos $\omega$ distributions. This yielded,

$$\frac{\alpha_o}{\alpha_-} = 0.977 \pm 0.071.$$

TABLE V

ASYMMETRY PARAMETERS AS A FUNCTION OF PRODUCTION ANGLE

| $\cos \Theta^*_\Lambda$ | $\alpha_o \bar{P} \pm \delta_o$ | $\alpha_- \bar{P} \pm \delta_-$ | $\alpha_o/\alpha_- \pm \Delta$ |
|---|---|---|---|
| -.7 | 0.364 ± .070 | 0.438 ± .079 | 0.832 ± .219 |
| -.5 | 0.479 ± .050 | 0.375 ± .039 | 1.280 ± .187 |
| -.3 | 0.491 ± .047 | 0.499 ± .031 | 0.984 ± .112 |
| -.1 | 0.550 ± .060 | 0.549 ± .037 | 1.002 ± .127 |
| +.1 | 0.450 ± .084 | 0.533 ± .055 | 0.844 ± .181 |
| +.3 | 0.315 ± .134 | 0.498 ± .100 | 0.632 ± .298 |
| +.5 | 0.567 ± .266 | 0.404 ± .300 | 1.406 ±1.234 |

Finally, this result was combined with the earlier measurement of Cork, et. al, to yield,

$$\frac{\alpha_o}{\alpha_-} = 0.985 \pm 0.069 \quad .$$

The $|\Delta \vec{I}| = \frac{1}{2}$ rule predicts that $\alpha_o/\alpha_- = 1.0$ in the absence of electromagnetic corrections. These effects have recently been calculated by Belavin and Narodetsky[8]. Their correction indicates that $\alpha_o$ should be a few percent larger than $\alpha_-$.

In summary, our result is in good agreement with the $|\Delta \vec{I}| = \frac{1}{2}$ rule.

## VI. CONCLUSION

It is now possible to determine the $|\Delta\vec{I}| = 3/2$ S and P-wave amplitudes allowed by the data explicitly. Our experiment, averaged with Cork's earlier measurement, has determined $\alpha_o/\alpha_-$ to be,

$$\frac{\alpha_o}{\alpha_-} = 0.985 \pm 0.069 \quad .$$

The best experimental value for $\alpha_-$ is[9],

$$\alpha_- = 0.65 \pm 0.02 \quad .$$

Substituting these values, along with the small final state corrections, into the equations (3) and (4) of Chapter II yields,

$$S_{11} = (0.940 \pm 0.005) \times (\Gamma^o + \Gamma^-)^{\frac{1}{2}}$$

and

$$P_{11} = (0.342 \pm 0.015) \times (\Gamma^o + \Gamma^-)^{\frac{1}{2}} \quad .$$

Thus,

$$\frac{P_{11}}{S_{11}} = 0.364 \pm 0.016 \quad .$$

Substituting this value into the linear expressions for the $|\Delta\vec{I}| = 3/2$ S and P-wave amplitudes derived in Chapter II yields,

$$\Delta\alpha = -1.56 \left(\frac{S_{33}}{S_{11}}\right) + 1.64 \left(\frac{P_{33}}{P_{11}}\right) \quad \text{and}$$

$$\Delta\Gamma = 1.85 \left(\frac{S_{33}}{S_{11}}\right) + 0.24 \left(\frac{P_{33}}{P_{11}}\right) .$$

Here $\Delta\alpha$ is the measured value of $\alpha_o/\alpha_-$ minus the predicted value. A similar definition holds for $\Delta\Gamma$, where the best experimental value for the branching ratio is $\Gamma^o/\Gamma^- = 0.550 \pm 0.019$[21]. Final state nucleon interactions have been included but have a very small effect and the uncertainties in the coefficients are small compared to the uncertainties in $\Delta\alpha$ and $\Delta\Gamma$.

In the absence of phase space and electromagnetic corrections, the $|\Delta\vec{I}| = \frac{1}{2}$ rule would predict $\alpha_o/\alpha_- = 1.0$ and $\Gamma^o/\Gamma^- = 0.5$. Substituting these values into the equations above yields:

$$\frac{S_{33}}{S_{11}} = 0.026 \pm 0.010$$

and

$$\frac{P_{33}}{P_{11}} = 0.016 \pm 0.036 .$$

Bevalin and Narodetsky[8] have recently calculated the radiative corrections and predict $\alpha_o/\alpha_- = 1.03$ and

$\Gamma^o/\Gamma^- = 0.485$. The uncertainty in calculating these corrections in difficult to estimate but could be as large as three percent. Substituting their values into the equations above yields:

$$\frac{S_{33}}{S_{11}} = 0.036 \pm 0.010 \quad \text{and}$$

$$\frac{P_{33}}{P_{11}} = 0.008 \pm 0.036.$$

With the Bevalin and Narodetsky corrections the data indicate a $S_{33}$ amplitude 3.6 standard deviations from zero. This deviation is primarily determined by the branching ratio measurements and particularly by the high precision measurement of Baltay, et al.. If one uses branching ratio values allowed by the experimental error of Baltay, et al., the $S_{33}/S_{11}$ ratio is changed by one standard deviation. It is thus important to check both the radiative calculations of Bevalin and Narodetsky and to test the results of Baltay, et al. by repeating the branching ratio experiment to greater accuracy.

In summary, our measurement of the $\alpha_o/\alpha_-$ ratio shows no violation of the $|\Delta\vec{I}| = \frac{1}{2}$ rule. When our value is used with the branching ratio determination to calculate the S and P $|\Delta\vec{I}| = \frac{3}{2}$ amplitudes, we find these amplitudes to be small, but allow a $|\Delta\vec{I}| = \frac{3}{2}$ S wave amplitude of five percent.

We have thus demonstrated the feasibility of checking the $|\Delta\vec{I}| = \frac{1}{2}$ rule in lambda decay by using the difficult $\Lambda^o \to n\pi^o$

decay mode. Indeed, it appears that this may be the most feasible way to provide the best check on the rule in hyperon decay.

## LIST OF REFERENCES


1. M. Gell-Mann and A. Pais, Proc. Intl. Conference on High Energy Physics at Glasgow (Pergamon Press, London, 1955) p. 324.

2. O.E. Overseth, Nonleptonic Weak Decay Processes, to be published in Proceedings of the International Conference on Symmetries and Quark Models (1969), Gordon and Breach Publishers.

3. B. Cork, L. Kerth, W.A. Wenzel, J.W. Cronin, and R.L. Cool, Phys. Rev. 100, 1000 (1960).

4. G. Källen, Elementary Particle Physics, (Addison-Wesley Publishing Company, Inc., Reading, Palo Alto, and London, 1964) pp. 471.

5. T.D. Lee and C.N. Yang, Phys. Rev. 108, 1645 (1957).

6. L.D. Roper, R.M. Wright, and B.T. Feld, Phys. Rev. 138, B190 (1965).

7. L.G. Pondrom, Phys. Rev. 160, 1374 (1967).

8. A.A. Belavin and I.M. Narodetsky, Soviet Phys.-Nuclear Phys. 8, 568 (1969). Using the formula given by these authors we find $\alpha_o/\alpha_- - 1 = +0.03 \pm 0.01$ rather than + 0.015 quoted in the article. The assigned error includes uncertainties in the hyperon spin parameters, but no uncertainty in the calculation.

9. O.E. Overseth and R.F. Roth, Phys. Rev. Letters 19, 391 (1967).

10. Particle Data Group, Rev. Mod. Physics 41, 109 (1969).

11. M.M. Block, et. al., Nuovo Cimento 28, 299 (1963). J. Cronin and O.E. Overseth, Phys. Rev. 129, 1795 (1963).

12. M.H. MacGregor, R.A. Arndt, and R.M. Wright, Phys. Rev. 173, 1272 (1968).

13. P.H. Bowen, G.C. Cox, G.B. Huxtable, J.P. Scanlon, J.J. Thresher, and A. Langsford, Nuclear Physics 30, 475 (1962).

14. L. Pondrom, S. Olsen, and J. Barney, Nucl. Instr. and Meth. 69, 282 (1969).

15. M.H. Hull, K.E. Lassila, H.M. Ruppel, F.A. McDonald, and G. Breit, Phys. Rev. 122, 1606 (1961).

16. A complete description of the Monte Carlo calculations is contained in S.L. Olsen, Thesis, University of Wisconsin 1970 (unpublished).

17. A. Saulys, D.I. Meyer, and R. Allen, Nucl. Instr. and Meth. 39, 335 (1966).

18. L. Hulthen, Handbuch der Physics 39, 141 (1957).

19. W.E. Cleland, et. al., Phys. Letters 26B, 45 (1967).

20. F. Harris, O.E. Overseth, L. Pondrom, and E. Dettmann, Phys. Rev. Letters 24, 165 (1970).

21. N. Yeh, C. Baltay, A. Bridgewater, W.A. Cooper, and M. Habibi, Bull. Am. Phys. Soc. 14, 94 (1969), and private communication, $\Gamma^- / (\Gamma^0 + \Gamma^-) = 0.647 \pm 0.009$. The value $\Gamma^0 / \Gamma^- = 0.55 \pm 0.019$ was obtained by combining this result and the average value of the Particle Data Group, Rev. Mod. Phys. 41, 109 (1969).